Journal of Hydrology 677 (2026) 135799

Contents lists available at ScienceDirect

Journal of Hydrology

journal homepage: www.elsevier.com/locate/jhydrol

High-resolution study of pollutant mobility in an acid mine drainage-impacted estuary under changing tidal and river contributions

Laura Sánchez-López [a,*], Jonatan Romero-Matos [a], Carlos R. Cánovas [a], Rémi Freydier [b], Rafael Pérez-López [a]

[a] Department of Earth Sciences & Research Center on Natural Resources, Health and the Environment, University of Huelva, Campus "El Carmen", E-21071 Huelva, Spain

[b] HydroSciences Montpellier (HSM), Université de Montpellier, CNRS, IRD, Montpellier, France

ARTICLE INFO

This manuscript was handled by D. Han, Editor-in-Chief, with the assistance of Martin Thullner, Associate Editor

Keywords:
Ría de Huelva estuary
Acid mine drainage
Seawater mixing
Partitioning
Tide-flow interactions

ABSTRACT

The present study investigates the behaviour of acid mine drainage (AMD)-derived contaminants in the Tinto River estuary (SW Spain) using five high-resolution (hourly) fixed-point sampling campaigns conducted under contrasting hydrological and tidal regimes: low-riverflow neap and spring tides, and high-riverflow events following rainfall across different tidal coefficients. Water chemistry and mineral phases were characterised using established analytical techniques and electron microscopy, while aqueous speciation and mineral saturation indices were evaluated through PHREEQC geochemical modelling. The results indicate that Mn, Zn, Co, Ni and Cd exhibit quasi-conservative behaviour, with low partition coefficients (Kd) and predominance in the dissolved phase. In contrast, Fe and Al sequentially precipitate as schwertmannite and basaluminite, respectively, dominating the suspended particulate matter (SPM) and acting as sinks for other metal(oid)s (As, Pb and Cu). Arsenic is initially removed under acidic conditions and remobilized when pH exceeds 6 due to desorption from schwertmannite. Lead exhibited a singular response, with episodically high dissolved concentrations under specific high-flow conditions, likely linked to sulfate-mineral solubility and evaporite washout in the fluvial basin. Low-flow conditions, particularly during spring tides, and highly diluted high-flow events reduce metal mobility by enhancing partitioning into SPM and deposition in the upper estuary (except for As). Conversely, less diluted high-flow conditions promote downstream transport and export to the Atlantic Ocean. This work provides the first tide-resolved and hydrologically contrasted assessment of contaminant dynamics in an AMD-impacted estuary and offers a transferable framework for predicting metal(loid) fluxes to coastal systems under increasing hydrological variability.

1. Introduction

Rivers are the primary vectors of solute transport from continental systems to coastal areas and ultimately oceans. Among the dissolved constituents, certain elements are classified as potentially toxic elements (PTEs), which have received increasing attention due to their deleterious effects on ecosystems, particularly estuarine environments. Throughout estuaries, pollutants can be incorporated into sediments, accumulate in organisms, or participate in reactions, determining their final destination. Although some of the estuarine inputs are naturally occurring, human activities — particularly mining, industry, farming, and urbanisation — have significantly increased the loads of PTEs delivered by rivers in recent decades (de Souza Machado et al., 2016).

Pollutant metal(oid)s released into the aquatic environment exhibit complex behaviour, influenced by physicochemical factors such as pH, salinity, the presence of organic matter, and redox dynamics. In estuaries, the confluence of fresh and marine waters produces dynamic fluctuations in these factors, which leads to a range of processes – including adsorption, coagulation, precipitation and redissolution – operating simultaneously (Achterberg et al., 2003; Asta et al., 2015; Zhang et al., 2015). Such processes strongly influence the mobility and bioavailability of pollutants. Therefore, estuaries play a key role as areas of metal transformation and retention, but also as potential gateways for metal input to the ocean.

In the context of anthropogenic pollution, acid mine drainage (AMD) represents one of the most persistent and environmentally concerning

* Corresponding author.
E-mail address: laura.sanchez@dct.uhu.es (L. Sánchez-López).

https://doi.org/10.1016/j.jhydrol.2026.135799
Received 22 January 2026; Received in revised form 11 May 2026; Accepted 28 May 2026
Available online 29 May 2026

pollution sources worldwide. It arises from the oxidative dissolution of sulphides upon exposure to oxygen and water, producing highly acidic solutions enriched in sulfate and metal(oid)s. Unlike most pollution sources, AMD generation can continue long after mining activities have ceased, impacting river systems, aquifers, and coastal environments (Leblanc et al., 2000; Nordstrom, 2011), as documented in several estuarine and fluvial systems, including the King River (Tasmania, Australia; Augustinus et al., 2010; Nascimento et al., 2023), Carnon River (Cornwall, United Kingdom; Braungardt et al., 2011; Jennings et al., 2025), Afon Goch (north Wales, United Kingdom; Dean et al., 2013), Chonam-ri Creek (South Korea; Jung et al., 2012), Dashu River (southwest China; Li et al., 2021), and Gromolo Torrent (Liguria, Italy; Consani et al., 2019). Among these, the Ría de Huelva Estuary (southwest Spain) stands out as one of the most AMD-polluted estuaries globally (Davis et al., 2000; Olías et al., 2006; Sánchez-Moyano et al., 2025), receiving acidic discharges from the Tinto and Odiel rivers that drain abandoned mining areas within the Iberian Pyrite Belt (IPB), one of the world's largest sulphide provinces with a mining history spanning approximately 5000 years (Davis et al., 2000; Leblanc et al., 2000). The metal load transported to the estuary and subsequently to the Atlantic Ocean is strongly controlled by highly irregular precipitation patterns (Cánovas et al., 2008), while the mixing of these acidic waters (pH 2–4) with alkaline seawater generates pronounced physicochemical gradients that strongly influence metal(oid) removal and release processes.

Despite the existence of prior research addressing the geochemistry of the Ría de Huelva Estuary (**e.g.,** Hierro et al., 2014a,b; Asta et al., 2015; Papaslioti et al., 2024), most studies have been limited in scope, focusing on specific estuarine conditions or restricted time scales. In particular, the influence of fortnightly (neap-spring) and daily (ebb-flood) tidal cycles on the pollutant distribution have only been partially documented, while the role of river flow regimes, especially those linked to rainfall events, remains poorly explored. Consequently, a significant knowledge gap persists regarding how hydrodynamic variability at different temporal scales – ranging from tidal to seasonal – modulates the geochemical processes controlling metal(oid) mobility and their ultimate fate in the ocean. In this sense, the gross flux of dissolved elements from the AMD-impacted Tinto and Odiel rivers, the main tributaries of the estuary, has been assessed in previous studies (**e.g.,** Olías et al., 2006; Nieto et al., 2013), which reported disproportionately high metal contributions relative to global riverine flux (e.g., 60% of Zn and 16% of Cu). However, upon entering the estuary, these metals undergo abrupt geochemical processes during their transfer to the ocean (Papaslioti et al., 2024), so that only certain fractions of gross flux reach marine waters in dissolved form (i.e., the net global flux). Hence, a comprehensive understanding of metal behaviour under varying estuarine hydrodynamic conditions is essential to improve estimates of net metal fluxes to the ocean.

Since estuarine processes operate over short temporal scales (hourly to daily), a site-specific high-resolution sampling approach within the estuary would be required to characterise metal(loid) dynamics and fate during the rapid geochemical processes induced by the mixing of highly acidic and metal-rich river waters with alkaline seawater. In this context, the main objectives of this work are: 1) to elucidate the geochemical factors controlling the behaviour of mining-derived pollutants as they traverse the Tinto River estuary, under the combined influence of tidal forcing and river hydrology; 2) to characterize partitioning between dissolved and particulate phases, which determines metal(oid)s transport, reactivity, and bioavailability within the estuarine environment; and 3) to discuss how contrasting estuarine hydrodynamics influence the net flux of AMD-derived pollutants. This study provides an integrated view of the geochemical mechanisms operating in an estuary subject to extreme conditions.

2. Material and methods

2.1. Study site

The Tinto River Estuary is governed by a semidiurnal mesotidal regime. The tidal range varies markedly, reaching ~ 4 m during spring tides and dropping to ~ 0.5 m during neap tides (Borrego et al., 2004). The climate of the area is Mediterranean-Csa type according to the Köppen classification, characterized by mild and wet winters and long warm to hot and dry summers. The mean annual temperature is 18.8 °C, and the average annual precipitation is 490 mm. The rainy season is commonly observed from November to January, while rainfall is practically non-existent during summer. Nevertheless, rainfall exhibits a high inter- and intra-annual variability, with long droughts and intense but short rainy periods. According to previous studies (e.g., Olías et al., 2006; Cánovas et al., 2008), the average flow of the Tinto River is 1.6 m^3/s. However, due to the absence of permeable rocks in the watershed and vegetation cover, the river flow exhibits high variability depending on the rainfall regime, ranging from 0.01 to more than 100 m^3/s during flood events. As a result, it experiences very rapid floods as well as a rapid decrease in flow as soon as the rains cease. Therefore, the river Tinto's discharge into the estuary is highly seasonal and inter-annually irregular.

2.2. Sampling

The Tinto River basin has been subject to intensive mining activity for approximately 5,000 years, although the greatest environmental impact occurred between the mid-19th and late 20th centuries (Davis et al., 2000**;** Leblanc et al., 2000). The mining sector's crisis in the 80 s and 90 s, driven by changes in global demand and economic factors, culminated in the widespread closure of sulfide mines by 2001 (Olías et al., 2006). The interruption of activity led to the shutdown of water pumping and treatment systems, thereby facilitating the generation and uncontrolled release of AMD, as evidenced by the deterioration of the geochemical conditions in the Tinto River and estuary (Olías et al., 2006). The reopening of some mines allowed water management systems to be re-established from the late 2000 s onwards, although the historical mine wastes have continued to impact the river chemistry (Olías et al., 2006). Furthermore, the Huelva estuary has historically received industrial discharges from the Industrial Complex, dominated by metallurgical, petrochemical and fertilizer industries, including large-scale deposits of phosphogypsum (~100 Mt) on the salt marshes downstream the estuarine sampling point (Fig. 1), which also generate acidic leachates enriched in pollutants. Although direct discharges have been reduced since the late 90 s, both AMD and phosphogypsum still contribute to the pollutant load into the estuary. However, the contribution of metal(oid)s from the industrial sector is between one and two orders of magnitude lower than that derived from mining activities (Pérez-López et al., 2011; Millán-Becerro et al., 2023). Regulatory-driven changes since the late 90 s have markedly improved estuarine water quality, with lower acidity and reduced concentrations of metal(oid)s (e.g., Fe, As, Pb) relative to historical conditions (Olías et al., 2006**;** Hierro et al., 2014b**;** Table SM1). Table SM1 compiles historical data from 1996 to 2018 (Elbaz-Poulichet et al., 1999; Braungardt et al., 2003; Achterberg et al., 2003; Cánovas et al., 2007; Hierro et al., 2014a, b; Papaslioti et al., 2024) and the present study (2023–2024) for comparison between the period of uncontrolled discharges and current conditions in the Tinto River and the estuary.

In order to study the tidal influence on the variation of physicochemical parameters and pollutant concentrations and loads in the Tinto River estuary, high-resolution samplings were carried out during different river and tidal conditions. The sampling point in the estuary is located at San Juan del Puerto (Huelva), within the fluvial domain of the Tinto River estuary (Fig. 1). Five sampling campaigns were conducted: (I) 29–30 March 2023 with low flow ($<1 m^3/s$) and neap tides (Tidal

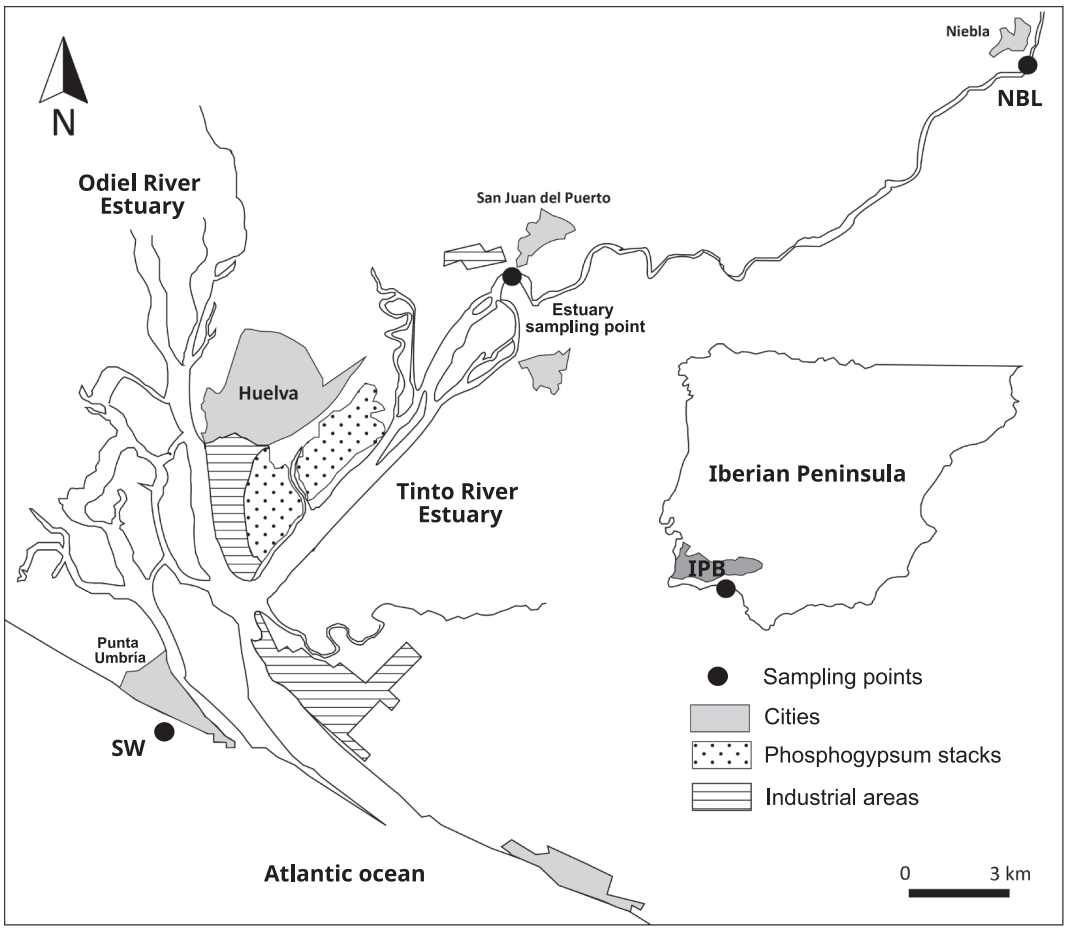

Fig. 1. Map of the study area showing the location of the sampling points in the estuary of the Tinto River, river end-member at Niebla (NBL) and seawater end-member (SW). IPB, Iberian Pyrite Belt.

Coefficient, TC 26–30); (II) 18–19 April 2023 with low flow (<1m^3/s) and spring tides (TC 99–102); (III) 22 January 2024 with high flow (8.6–12.8 m^3/s) after a rain event and intermediate tides (TC 59–62); (IV) 12–13 February 2024 with very high flow (18.8–42.91 m^3/s) after a more intense rain event and spring tides (TC 105–95); and (V) 19–20 February 2024 with high flow (4.6–6.7 m^3/s) and neap tides (TC 43–53). The flow and rainfall data were obtained from a gauging-pluviometric station, located about 20 km upstream from the sampling point (Fig. SM2), within the SAIH-Hidrosur network of the regional government (redhidrosurmedioambiente.es). Samples were collected using a Teledyne ISCO® autosampler programmed with a frequency of one sample per hour during 24 h for samplings I, II, IV and V; and one sample every 30 min during 12 h for sampling III (n = 120). The autosampler was equipped with 24 polyethylene bottles (capacity of 1 L) that were previously washed in 10% (v/v) HNO_3 and rinsed in Milli-Q water. To avoid cross-contamination purge sequences between pumping cycles were scheduled. After collection, samples were processed in the laboratory and then refrigerated. For each sampling campaign, water samples were collected from the Tinto River at Niebla (NBL), upstream of the tidal influence (Fig. 1). In addition, a seawater sample (SW) representing the marine end-member was collected at the Atlantic coast (Fig. 1).

For each sample, pH, temperature, oxidation–reduction potential (ORP), and electrical conductivity (EC) were measured using a portable multi-parameter electrode (Hanna® instruments, HI9025 and HI9033). Prior to undertaking EC and pH measurements, the equipment was calibrated at three points (147 µS/cm, 1413 µS/cm, and 12.88 mS/cm and 4.01, 7.00, and 9.21, respectively). In addition, ORP was controlled using two standard solutions (220 and 470 mV). Alkalinity was determined by CHEMetrics® Total Titrets®, with a range of 5–100 mg L^{-1} as $CaCO_3$ equivalents. Additionally, water level was monitored in situ using a datalogger CTD-Diver® installed at the estuarine sampling point.

2.3. Analytical methods

2.3.1. Liquid phase characterization

Aliquots for cations determination were filtered through 0.45 µm Millipore Teflon filters, acidified with ultrapure HNO_3 (1% v/v) Merck to pH < 2, and stored in the dark at 4 °C until analysis. Also, unfiltered aliquots were taken and acidified to determine the proportion of metals associated with the dissolved and particulate fraction, following the procedure of Garbarino and Hoffman (1999). Aliquots for anion determination were filtered but not acidified. The dissolved fraction (%D) for each element was calculated as follows:

$$\%D = \frac{100[Cdissolved]}{[Ctotal]}$$

where *C dissolved* corresponds to the concentration in the filtered water aliquots (mg/L or µg/L) and *C total* is the concentration in unfiltered aliquots (mg/L or µg/L).

The concentrations of major elements were measured using Inductively Coupled Plasma-Optical Emission Spectroscopy (ICP-OES, Jobin Yvon Ultima 2) at the Research and Development Services of the University of Huelva. The concentrations of trace elements were determined by Inductively Coupled Plasma-Mass Spectrometry (ICP-MS) with a Thermo Scientific iCAP TQ ICP-MS at the "Plateforme AETE-ISO" (OSU OREME, University of Montpellier) without any prior dilution using Kinetic energy Discrimination – Argon Gas Dilution (KED-AGD mode).

To address signal drifts during trace element determinations, an internal solution comprising Be, Sc, Ge, Rh, and Ir was introduced online to the samples. Estuarine water and seawater reference materials for trace metals (SLEW-3 and CASS-6) were also analyzed to check the analytical accuracy, which was within 10% of the certified values. Detection limits were between 0.02 and 0.20 mg/L for major elements and from 0.23 ng/L (Zn) to 3.44 ng/L (La) for trace elements. Anions (Cl^-, F^-, Br^-, SO_4^- and PO_4^-) were determined by High-Performance Liquid Chromatography (HPLC; Dionex DX-120) with a 4 × 250 mm column (AS 9-HC) and a 4 mm suppressor membrane (ASRS-ULTRA) at the Research and Development Services of the University of Huelva.

2.3.2. Solid phase characterization

The suspended particulate matter (SPM) was measured by weighing the particulate matter retained on the 0.45 μm filters. The vacuum filtration technique was used to separate the SPM from water employing a kitasato flask, a funnel, and a beaker pre-decontaminated. A volume of 0.5 L from each sample was filtered to obtain the mg/L of SPM. Before use, each filter was oven-dried and weighted. Once each sample was processed, the filters were oven-dried (40 °C, 24 h) and cooled in desiccators before being weighted. The amount of SPM retained in the filter was calculated as the difference between the final and initial weight. The particulate matter accumulated on the filters was mineralogically characterized by Field Emission Scanning Electron Microscopy (FESEM, JEOL IT-300HR-LV) for imaging and Energy-Dispersive X-ray (EDX) for qualitative chemical analyses at the Research and Development Services of the University of Huelva. In addition, 15 filters from samplings III–V were selected for semi-total digestion, as sufficient matter was available only during these campaigns to determine the bulk chemical composition. The digestion was carried out using aqua regia ($HCl:HNO_3$, 3:1) in PTFE vessels (Savillex®), heated at 90 °C for 2 h in an oven. After digestion, the samples were cooled to room temperature and subsequently evaporated on a hot plate at 55 °C. The resulting dry residue was then redissolved in 2.5 mL of HNO_3 and Milli-Q grade distilled water, and the solution was brought to a final volume of 50 mL to obtain a 5% acidified solution. This final aliquot was analyzed using both ICP-OES and ICP-MS techniques.

The partition coefficient (Kd, L/kg) between the dissolved (<0.45 μm) and particulate phases (>0.45 μm) was determined to assess the mobility and geochemical behaviour of the contaminants under estuarine mixing conditions, as follows:

$$Kd = \frac{C\,\text{particulate}}{C\,dissolved}$$

where *C* particulate is the concentration in suspended particulate matter (mg/kg) and *C* dissolved corresponds to the concentration in the filtered water fraction (mg/L).

2.4. Geochemical and mixing models

The geochemical modelling software PHREEQC-3.0 (Parkhurst and Appelo, 2013) was used for speciation and solution/reaction calculations, employing the *Thermoddem.dat* thermodynamic database (Blanc et al., 2012). The database was expanded with equilibrium constants of schwertmannite $[Fe_8O_8(OH)_{8-2x}(SO_4)_x{\cdot}nH_2O]$ from Sánchez-España et al. (2011) and basaluminite $[Al_4(OH)_{10}(SO_4){\cdot}nH_2O]$ and $Al(OH)_3(a)$ from *Wateq4f.dat* database (Ball and Nordstrom, 1991). To enable accurate modelling, Eh values were adjusted to pe values referenced to the standard hydrogen electrode (Nordstrom and Wilde, 1998). PHREEQC code was used to model the aqueous speciation of estuarine and river solutions, and to calculate the saturation indices (SI) of relevant mineral phases controlling estuarine geochemical processes (e.g., schwertmannite and basaluminite). In addition, to estimate the seawater fraction (SWf) during the estuarine mixing, the statistical mixing model MIX (Carrera et al., 2004) was employed. This model facilitates the calculation of the mixing ratios of fluvial and marine waters considering the uncertainty in end-member concentrations by a maximum likelihood method. The calculations were based on dissolved concentrations of conservative elements (Cl, Na, Ca, Mg and K) that exhibited substantial variation between river and sea water.

3. Results and discussion

3.1. End-members characterization

Table 1 presents the dissolved element concentrations and the corresponding physicochemical parameters at the fluvial end-member (NBL), and the marine end-member (SW). The physicochemical parameters of river water exhibited clear variations between low- and high-flow conditions, with subsequent implications for contaminant concentrations. During low-flow campaigns (I and II), pH values were highly acidic (2.29–2.63), accompanied by elevated EC values (ca. 2.80 mS/cm) and high Eh values (550–567 mV). During the dry season, reduced river discharge and limited freshwater input result in lower pH, higher EC and increased element concentrations at the NBL site. In contrast, under high-flow conditions (III, IV, and V), pH increased to less acidic levels (2.94–3.41), while EC (0.74–1.51 mS/cm), Eh (440–517 mV) and element concentrations markedly decreased, reflecting the greater influence of freshwater dilution.

In the Tinto River, Fe and Al dominate the metal concentrations across the five sampling campaigns (Table 1). Iron concentrations were consistently higher than those of Al, with a range of 1.4 to 2.6 times greater. The concentrations of Cu, Zn, and Mn were approximately 7 to 10 times lower than those of Fe. Trace elements followed the order Zn > Cu > Mn > Co > Ni > Cd > Pb > As. Localized anomalies were observed during sampling III, particularly in the case of Pb, which reached unusually elevated concentrations compared to the other samplings, an aspect further discussed in next sections. Overall, metal(oid)s were predominantly present in the dissolved phase in the five samples (%D > 80), except for As in samples NBL-III and NBL-V, where the percentage

Table 1
Physicochemical parameters and chemical composition of the dissolved phase of samples corresponding to the Tinto River end-member at Niebla (NBL) for the five sampling campaigns, and the marine end-member (SW). Alk, alkalinity; n.a.d., non-available data; d.l., detection limit.

		NBL-I	NBL-II	NBL-III	NBL-IV	NBL-V	SW
pH		2.63	2.29	3.03	3.41	2.94	8.14
EC	mS/cm	2.83	2.84	1.18	0.74	1.51	57.3
Eh	mV	567	551	459	440	517	238
Alk	mg/L eq. $CaCO_3$	0.00	0.00	0.00	0.00	0.00	140
Cl-	mg/L	51.6	95.1	46.4	34.7	34.1	22,762
Br-	mg/L	1654	1804	469	267	1107	75.7
SO_4^{2-}	mg/L	1544	1762	543	185	742	2905
Ca	mg/L	68.5	82.4	24.0	12.6	32.0	351
K	mg/L	6.39	6.90	27.3	6.37	9.53	446
Mg	mg/L	87.2	95.9	32.7	12.4	44.1	n.a.d
Na	mg/L	44.7	55.6	19.3	10.7	23.5	10,346
Fe	mg/L	159	147	63.0	13.3	54.5	<d.l.
Al	mg/L	87.1	88.4	24.0	8.08	39.1	<d.l.
Mn	mg/L	8.83	9.20	2.79	0.83	3.45	1.98
Cu	mg/L	17.0	17.1	6.01	1.61	7.59	<d.l.
Zn	mg/L	17.2	18.3	7.30	1.81	7.60	<d.l.
Sr	mg/L	0.22	0.30	0.07	0.04	0.10	8.17
Li	μg/L	137	143	44.7	19.4	71.9	169
B	μg/L	n.a.d	n.a.d	26.4	21.9	42.0	5534
Co	μg/L	531	620	190	53.0	243	<d.l.
Ni	μg/L	118	130	32.2	13.0	44.2	0.84
As	μg/L	35.5	21.5	7.67	1.09	3.01	1.70
Cd	μg/L	73.4	75.9	29.4	7.76	33.3	<d.l.
Ba	μg/L	15.0	14.4	15.2	8.98	18.2	6.40
Pb	μg/L	34.9	32.0	233	30.1	46.8	0.22

in the dissolved phase was 40% and 63%, respectively. Previous studies have similarly reported that metal(loid)s in the Tinto River are mainly transported in dissolved form, although association with Fe-rich colloids and other particulate phases may occur during high-flow conditions (e.g., Cánovas et al., 2012; Olías et al., 2020; Papaslioti et al., 2024). While low-flow samples exhibit more acidic conditions and contain contaminants mainly in solution, high-flow samples are slightly less acidic and show saturation indices for Fe oxyhydroxysulfates, mainly schwertmannite, close to equilibrium. This suggests that precipitation may occur according to PHREEQC calculations, or that equilibrium conditions were reached upstream, coupled with iron precipitation. In fact, the high affinity of schwertmannite for As at acidic pH values is well known in similar acidic environments worldwide (e.g., Carlson et al., 2002; Fukushi et al., 2003; Asta et al., 2010; Parviainen et al., 2015), which is consistent with the observed association of As with the particulate fraction in these samples, as discussed in later sections. Overall, these results fall within the historical range of the Tinto River, characterized by acidic pH and high sulfate and metal(oid) concentrations (see Table SM1).

In contrast to the acidic fluvial end-member, the marine end-member exhibits alkaline pH and high EC values (i.e., pH 8.14; 57.3 mS/cm), presenting significant alkalinity (140 mg/L eq. $CaCO_3$). The chemical composition is dominated by major ions of marine origin (i.e., Cl^-, Na^+, SO_4^{2-}, Ca^{2+}, K^+, Sr^{2+}, B^+, Li^+), while the concentrations of metal(oid)s remain very low or below detection limits, highlighting the role of seawater end-member as a key driver of dilution of metal(oid)s during estuarine mixing and/or promoting their precipitation due to pH changes.

3.2. Estuarine physicochemical conditions and dissolved contaminant concentrations

Table 2 shows the main physicochemical parameters and dissolved chemical composition of the samples collected in the estuary, and Fig. 2 shows the fluctuations of the seawater fraction (SWf), water level, pH, and EC during all samplings. Complete dataset for the estuarine samples is provided in Table SM3.

The observed values are consistent with the reported ranges for estuarine mixing conditions in previous studies (see Table SM1), except for Pb, which will be discussed below. Oscillations of pH and EC observed across the tidal cycles of all sampling campaigns (I to V) clearly reflect the progression of tidal stages, exhibiting elevated values during flood tides and diminished values during ebb tides (Fig. 2). Nevertheless, pH and EC exhibit considerable variability between samplings. Electrical conductivity values during low river discharge (I and II) reflect stronger marine influence reaching similar values to those of seawater (≈50 mS/cm). Conversely, EC during high river discharge (III, IV and V) reflects stronger riverine influence, exhibiting values ranging from 1.57 to 31.5 mS/cm. For low river discharge and high seawater proportion (samplings I and II, SWf > 0.5), pH values fluctuate reaching neutral values (pH≈7) in flood tides. For high river discharge and low proportion of seawater (samplings III and V, SWf < 0.5), pH values remained

Table 2
Physicochemical parameters and chemical composition of the dissolved phase in the samples collected in the Tinto River estuary during the sampling campaigns (mean; median). Alk, alkalinity; n.a.d non available data, d.l. detection limit.

		I		II		III		IV		V	
pH		4.00–6.29	(5.03; 4.92)	4.47–7.68	(6.33; 6.76)	3.19–4.72	(3.60; 3.34)	4.11–6.37	(5.19; 4.92)	3.15–5.26	(3.87; 3.41)
EC	mS/cm	43.2–51.9	(47.7; 47.6)	43.7–53.0	(50.0; 51.0)	1.57–25.5	(10.8; 7.98)	1.95–16.9	(5.91; 4.30)	5.41–31.5	(17.8; 15.5)
Eh	mV	270–375	(324; 324)	221–318	(262; 252)	268–450	(401; 438)	190–349	(249; 256)	261–504	(406; 457)
Alk	mg/L eq. $CaCO_3$	0.00–23.0	(5.21; 2.50)	0.00–85.0	(36.3; 28.5)	0.00–0.00	—	0.00–70.0	(11.0; 0.00)	0.00–15.0	(0.63; 0.00)
Cl-	mg/L	13757–17236	(15569; 15493)	15357–20600	(18641; 19153)	267–10394	(4436; 3430)	428–5342	(1726; 1162)	1414–10557	(5803; 4902)
SO^{4-}	mg/L	2451–2757	(2627;2635)	2592–11481	(3128; 2730)	415–1361	(777; 675)	290–1052	(450; 375)	762–1924	(1252; 1133)
Fe	mg/L	<d.l.–3.56	(1.12; 0.57)	<d.l.–2.20	(0.34; —)	6.08–34.8	(22.2; 24.9)	0.00–12.5	(4.86; 5.05)	0.26–22.5	(8.60; 8.70)
Al	mg/L	<d.l.–11.8	(4.42; 3.41)	<d.l.–9.70	(1.75; —)	3.55–21.2	(14.2; 16.1)	0.00–10.9	(3.41; 1.95)	0.66–30.0	(14.7; 16.6)
Mn	mg/L	0.60–2.14	(1.39; 1.52)	0.13–2.00	(0.75; 0.58)	0.00–1.98	(1.35; 1.60)	0.37–1.21	(0.74; 0.73)	0.84–2.82	(1.77; 1.87)
Cu	mg/L	0.10–2.55	(1.21; 1.37)	0.03–1.31	(0.35; 0.14)	1.01–3.69	(2.46; 2.63)	0.01–2.07	(0.75; 0.65)	1.21–5.54	(3.15; 3.40)
Zn	mg/L	0.75–3.46	(2.14; 2.19)	0.09–3.00	(1.01; 0.67)	2.16–8.26	(5.34; 5.57)	0.32–4.00	(1.94; 1.91)	2.08–9.53	(5.06; 5.27)
Sr	mg/L	7.13–9.57	(8.39; 8.45)	7.40–10.4	(9.35; 9.50)	0.15–3.64	(1.39; 0.98)	0.22–2.33	(0.74; 0.53)	0.70–4.98	(2.67; 2.16)
Li	µg/L	132–162	(147; 148)	143–175	(159; 160)	32.5–96.2	(53.6; 45.4)	12.0–71.2	(35.3; 34.9)	56.8–114	(81.0; 72,9)
B	µg/L	3.16–4.01	(3.63; 3.61)	3.58–4.41	(4.07; 4.15)	0.09–2.22	(0.85; 0.62)	0.17–1.36	(0.53; 0.41)	0.39–2.45	(1.40; 1.18)
Co	µg/L	29.1–87.8	(56.9; 57.8)	5.55–78.3	(30.7; 27.1)	48.4–119	(86.6; 93.0)	15.1–65.5	(36.2; 34.9)	49.6–167	(100–107)
Ni	µg/L	10.1–23.4	(16.3; 16.4)	4.05–54.2	(12.4; 9.76)	14.7–32.9	(23.7; 24.9)	5.72–17.4	(11.6; 11.9)	11.6–36.5	(22.5; 23.1)
As	µg/L	0.93–3.45	(2.21; 2.12)	1.26–20.3	(7.39; 3.04)	0.93–4.47	(1.87; 1.76)	0.73–9.14	(2.78; 2.79)	0.34–1.69	(0.84; 0.79)
Cd	µg/L	7.60–14.4	(10.8; 10.5)	4.46–12.6	(7.69; 7.35)	7.26–23.1	(15.6; 16.9)	3.71–15.0	(8.53; 8.21)	9.30–34.4	(19.9; 38.1)
Ba	µg/L	18.1–20.0	(19.2; 19.2)	15.5–21.0	(18.8; 19.3)	18.2–22.9	(20.5; 20.7)	7.07–16.0	(13.7; 14.3)	15.5–17.6	(16.7; 16.7)
Pb	µg/L	0.46–24.4	(11.1; 12.2)	<d.l.-25.9	(6.21; 1.58)	98.8–442	(290; 343)	0.05–41.3	(14.4; 11.00)	7.57–70.2	(38.1; 41.7)

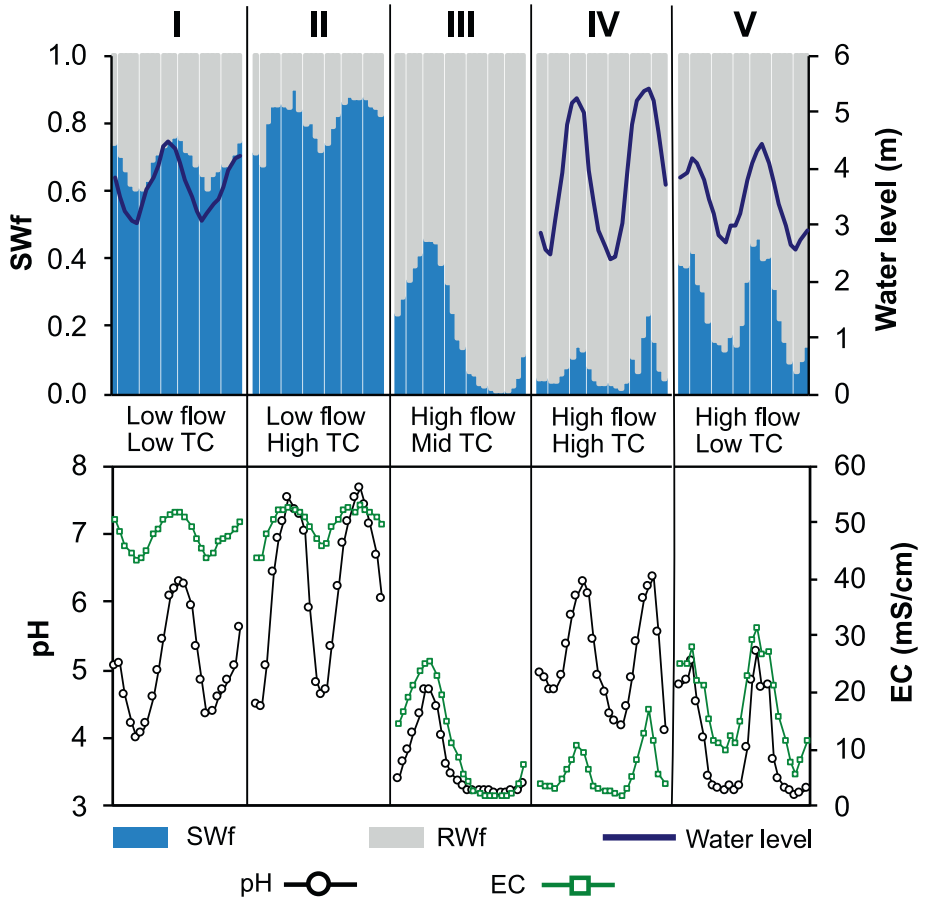

Fig. 2. Seawater fraction (SWf), river water fraction (RWf), water level, pH, and electrical conductivity (EC) recorded during the five sampling campaigns. Water level data is not available for campaigns II and III.

consistently acidic without reaching neutrality. In contrast, sampling IV, also with high river discharge, exhibited a pH range of 4.11–6.37, comparable to that of sampling I (i.e., 4.00–6.29), despite the much lower SWf recorded in IV (SWf < 0.3). Therefore, sampling IV represents a distinct scenario, where high discharge coincided with diluted riverine inputs, likely due to local intense rainfall dilution effect. Alkalinity tends to increase during high tide, reaching their maximum during this phase. At low tide, the higher proportion of acidic river water leads to a total depletion of alkalinity. In sampling III, no alkalinity was detected in any of the samples analysed, probably due to the low pH range recorded (i.e., 3.2–4.3). Conversely, quantifiable alkalinity values were recorded in the rest of the sampling campaigns (Table 2). The highest Eh values were consistently recorded at ebb tide in all sampling campaigns.

The dissolved concentrations of the analyzed elements are presented in Table 2, which summarizes their range, mean, and median values. Complete datasets for each sampling campaign are provided in Supplementary Material (Table SM3). Dissolved contaminants exhibited similar behaviour over all the tidal cycles recorded in all samplings. Dissolved concentrations reach their highest values during the ebb tide when the river's influence is maximum (lowest SWf values), excepting As that will be discussed later in the next section (Fig. 3). The influence of hydrological conditions on the input of dissolved metal concentrations becomes evident when comparing samplings upon different flow regimes. During low-flow conditions (I and II), when SWf remained above 0.5 across all the samples, concentrations were lower. In contrast, during high-flow conditions (III and V), characterized by SWf < 0.5, concentrations were consistently higher. Unlike the other high-discharge campaigns, sampling IV (SWf < 0.3) constitutes an exception of this trend, as intense rainfall diluted river inputs and led to markedly reduced dissolved metal(oid) concentrations in the estuary. These patterns highlight the combined influence of seawater mixing and freshwater contributions in shaping estuarine metal(oid)s dynamics. The higher the concentrations and acidity in the river end-member, the greater the seawater fraction is required to neutralize acidity, dilute or precipitate metal(oid)s (Fig. 3). Consequently, the observed decrease pattern in dissolved contaminant concentrations results from the combined effects of estuarine mixing and the initial geochemical characteristics of the riverine input, consistent with findings from previous research (e.g., Heidari, 2019; Hadikhani et al., 2024).

The relative abundance of dissolved metal(oid)s varied according to river discharge conditions. Under low-discharge conditions, dissolved Fe concentrations were similar to those of Cu, Zn and Mn, while Al dominated, reaching values up to five times higher than Fe. Conversely, during high-discharge conditions, Fe prevailed over Al, reproducing the pattern observed in the fluvial end-member (Table 2, Fig. 3). This pattern, and its geochemical significance, will be examined in more detail in the next section. The trace metal and metalloid hierarchy remained consistent across all campaigns, following the order Zn > Cu > Mn > Co > Pb > Ni > Cd > As.

The concentrations of dissolved Pb in sampling III were, as in NBL-III, six times higher than in the other samplings. Previous research conducted in the Tinto and Odiel river basins indicates that, Pb often shows a positive relationship with increasing river flow during rainfall events, while the others tend to be diluted (**e.g.,** Cánovas et al., 2007; Moreno-González et al., 2022). Some studies have attributed the distinctive behavior of Pb to the solubility control exerted by sulfate minerals (e.g., anglesite, Pb-jarosite) in AMD sources (e.g., waste dumps) and in evaporitic sulfate salts precipitated during the dry periods along riverbeds (Harris et al., 2003; Cánovas et al., 2007, 2010; Basallote et al., 2019). Other works have proposed that Pb is released through

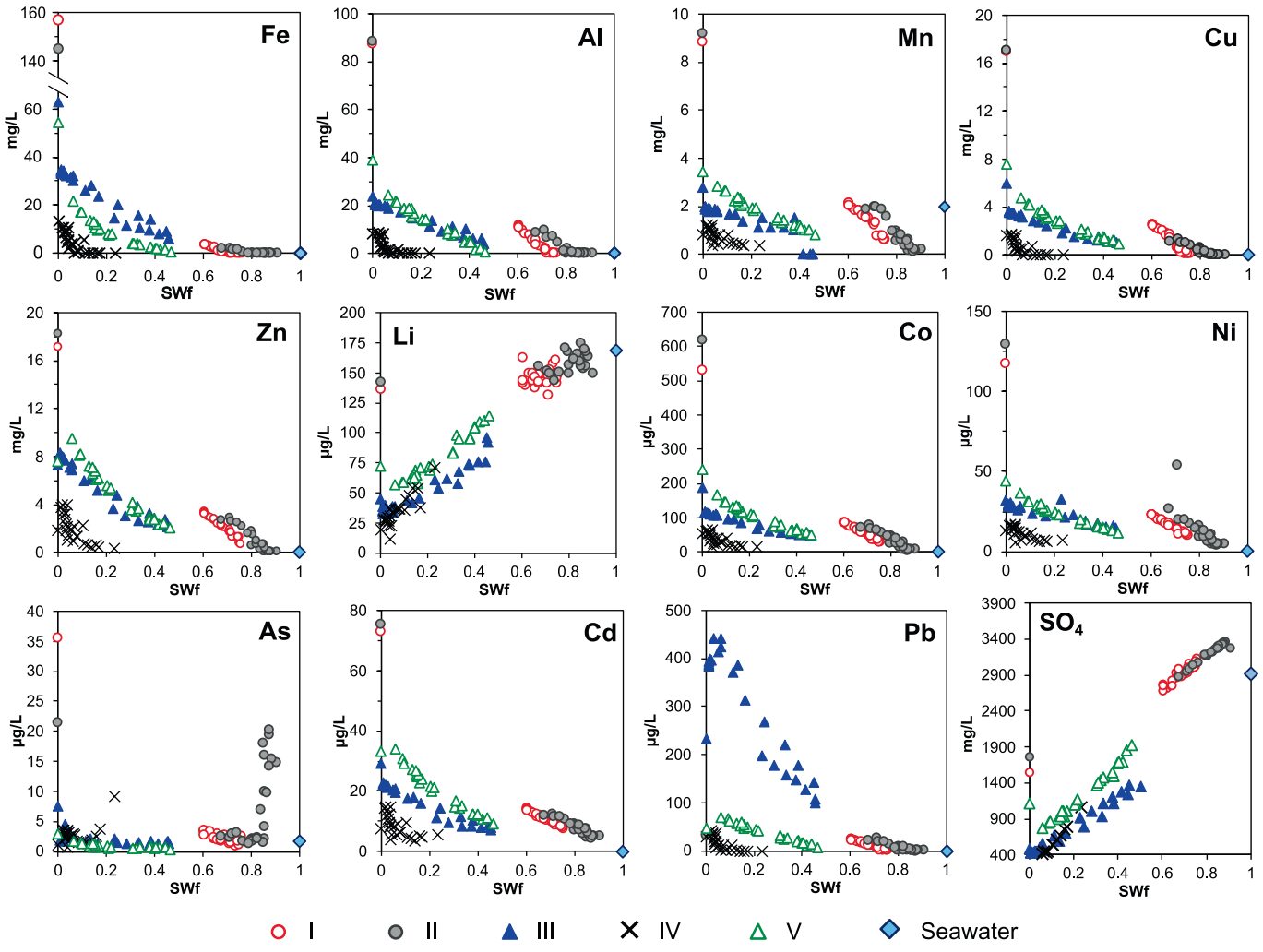

Fig. 3. Dissolved concentration of contaminants with seawater fraction (SWf).

desorption or transformation of Fe oxyhydroxysulfates (Acero et al., 2006; Sarmiento et al., 2009; Ram et al., 2021). Cánovas et al. (2010) also observed a shift in Pb behaviour in the upper Tinto River at the end of an evaporitic salt washout, which they attributed to the dominance of schwertmannite precipitation over jarosite, thereby decreasing Pb affinity through coprecipitation or adsorption into jarosite. Given that sampling III was performed following a brief drought and subsequent rainfall (Fig. SM2), it is plausible that the observed Pb pattern reflects the late stages of an evaporitic salt washout. However, further exploration is required to elucidate the implications of such events within the

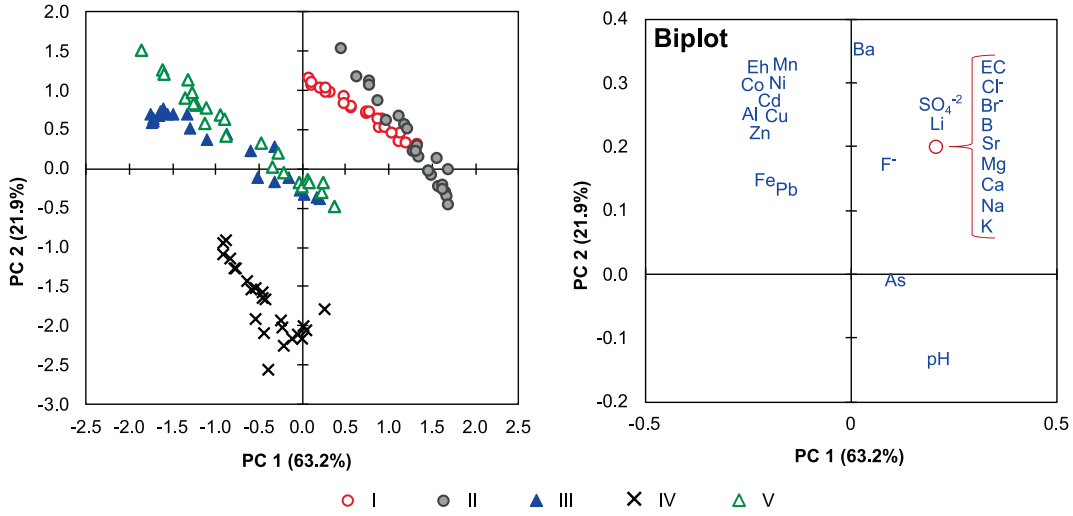

Fig. 4. Results obtained from the Principal Component Analysis (PCA).

Tinto River estuary as Pb is considered a concerning PTE. These findings highlight the need for continuous monitoring of estuarine mixing zones, particularly after rainfall events, to better assess contaminant fluxes reaching the Atlantic Ocean.

To study relationships among samples and variables, various Principal Component Analysis (PCA) of the results has been conducted. Given that certain variables do not demonstrate a normal distribution, Spearman's correlation matrix has been utilised for the PCAs (Davis, 2002). The PCA including samples from all five sampling campaigns (Fig. 4), explained 85.1% of the variance in the first two components (PC1 = 63.2%, PC2 = 21.9%). Clear groupings of samples were observed based on the river flow regimes. Samples corresponding to low-flow conditions (samplings I and II) were grouped in the upper right quadrant, suggesting a relatively homogeneous chemical composition under low river discharge conditions. Otherwise, high-flow samplings III and V formed distinct clusters in the top left quadrant, while sampling IV exhibited a different pattern, clustering in the bottom left quadrant. The PC1 reflects a fluvial-to-marine gradient, with increasing marine influence toward the right, whereas PC2 captures differences in contaminant concentration, decreasing from top to bottom. The low position of campaign IV in this space supports its interpretation as a high-flow event marked by rainfall-induced dilution of dissolved metals. These results suggest that the observed variability in chemical composition among sampling campaigns is strongly influenced by the hydrological regime. Moreover, high-flow events can trigger distinct geochemical responses. Similarly, in the individual PCA sample grouping was largely controlled by the relative contribution of marine and fluvial end-members, as reflected by PC1, which explained more than 90% of the total variance in each analysis (Fig. SM4). This pattern supports the previous results highlighting that tidal dynamics exert a strong short-term control over the composition of the Tinto estuary consistent with findings from other contaminated estuaries (**e.g.,** Nascimento et al., 2021; Cereja et al., 2022).

3.3. *Pollutant behaviour during the mixing*

The evolution of total (dissolved + particulate) versus dissolved concentrations of some pollutants during the mixing process between acidic river water and seawater across the tidal cycles recorded in the five samplings is shown in Fig. 5 and Fig. SM5. The elemental concentrations are also expressed as relative percentage in the dissolved phase with respect to the total concentration (%D) to evaluate their partitioning. The results show that sulfate, Zn, Co, Ni, and Cd were predominantly found in the dissolved fraction (%D > 80) through the five samplings (e.g., Zn in Fig. 5), mostly suggesting a quasi-conservative behaviour during the tidal cycles. The decrease in their total concentrations may be primarily associated with the seawater dilution effect, having minimal involvement in mineral precipitation and sorption processes as described in previous studies (**e.g.,** Pérez-López et al., 2023; Papaslioti et al., 2024). Conversely, Fe, Al, Cu, Pb and As exhibit a non-conservative behaviour pattern during tidal cycles (Fig. 5). These metal (oid)s undergo changes in phases distribution during tidal variations, with a general reduction in their proportion in the dissolved fraction during flood tide when marine influence reaches its maximum.

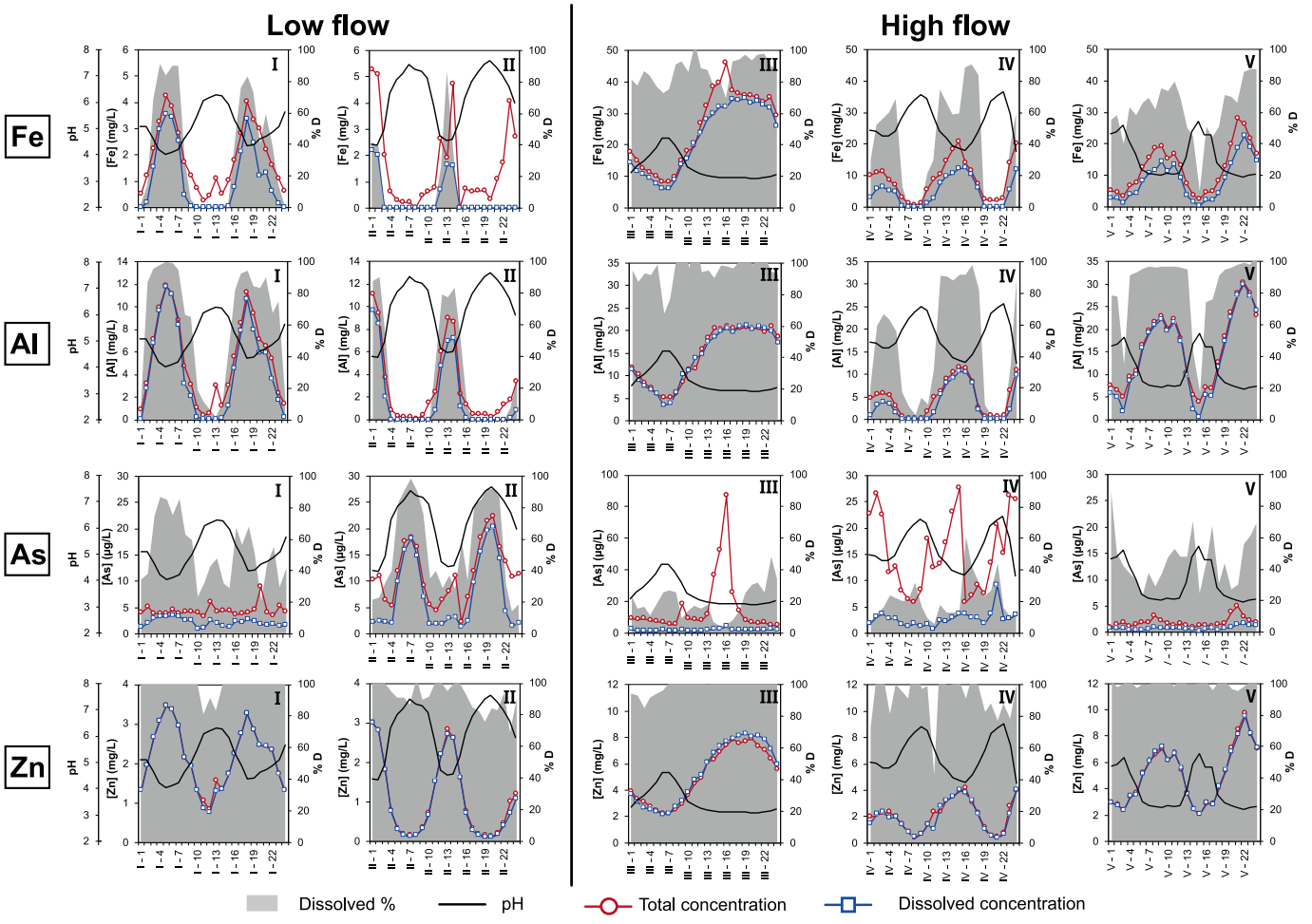

Fig. 5. Evolution of pH, total concentration, dissolved concentration and dissolved percentage of Fe and As over the tidal cycles recorded in the five sampling campaigns.

Consequently, the particulate concentration of these metal(oid)s tends to increase during this tidal phase. The decrease in their total concentrations appears to be due not only to marine dilution, but also to mineral precipitation processes that control their solubility.

In samplings I, II, IV and V, dissolved concentrations of Fe and Al dropped abruptly under detection limits during high tides. In contrast, their total concentrations, despite experiencing a significant decrease due to marine dilution, remain above the detection threshold. This divergence implies a change in the phase distribution, with a decrease in dissolved phase from initial values of 80–90% at the beginning of the rising tide to 0–20% when the pH peaks, observing a high positive correlation between Fe-Al removal and pH. During the estuarine mixing, iron is removed from solution earlier than Al, as reflected in Fig. 5 by the grey shading representing the dissolved percentage. This sequential precipitation is attributed to the different geochemical behaviour of Fe and Al under varying physicochemical conditions. Iron may precipitate at pH ~ 2.5–4.0, likely as schwertmannite [$Fe_8O_8(OH)_6(SO_4)\cdot nH_2O$], whereas aluminium precipitates at higher pH (~4.5–6.5), likely as basaluminite [$Al_4(SO_4)(OH)_{10}\cdot 4\text{-}5H_2O$], once Fe(III) removal is complete, which agrees with other studies **(e.g.,** Lozano et al., 2020; Pérez-López et al., 2023). In fact, according to the saturation indices obtained in PHREEQC, samples above pH 4, predominantly during high tide, were supersaturated with regard to schwertmannite and basaluminite (Table SM6; Fig. SM6). Otherwise, these precipitation processes are less noticeable in sampling III where Fe and Al were mainly in the dissolved phase (%D > 70). This is likely attributable to the lower variability in pH, with values only exceeding 4 in six samples during the high tide (Fig. 5).

The sequential precipitation of Fe and Al can also explain the relative higher abundance of Al over Fe during low-discharge periods in the estuary. During the first stages of the mixing Fe may have precipitated in the upper part of the estuary, upstream of the sampling point, while Al remained in solution. Conversely, reduced water residence time and lower pH range during high river discharges can limit the precipitation of Fe, allowing a larger fraction to remain in the dissolved phase until it reaches the sampling point, hence favouring Fe solubility.

A similar pattern is followed by Pb and Cu, which significantly reduce their proportion in the dissolved phase during flood tides when pH is above 5, as evidenced by samplings I, II and IV (Fig. SM5). In this case, no oversaturation with respect to mineral phases containing these metals was observed in PHREEQC modelling and their removal could therefore be attributed to adsorption and/or coprecipitation processes onto Fe and Al mineral phases (Lozano et al., 2020; Montecinos et al., 2022**).** Compared to Pb, Cu exhibits higher mobility: when its dissolved fraction decreases to ~ 20%, Pb is almost entirely removed from solution. This different trend is more evident in campaign II, where pH > 6.5 and higher SWf values were recorded. Under these conditions, Cu showed a singular behaviour, with its dissolved fraction remaining above 40% during both high tides, likely due to the formation of soluble Cu–chloride complexes (Hierro et al., 2014a; Abdou et al., 2022). PHREEQC speciation results supports this fact, identifying $CuCl_2^-$ as a dominant species under these conditions.

Arsenic exhibited a non-conservative "on–off" behaviour throughout the tidal cycles, being initially retained and later released back into solution. Under low-flow conditions (samplings I and II), As was initially removed from the dissolved phase during the rising tide. When pH values exceeded 6, however, a sharp release of As back into the dissolved phase was recorded. This effect was especially marked in flood-tide samples of campaign II, where dissolved concentrations nearly reached 100%, approaching those of the river end-member ([As] NBL-II = 21.5 µg/L) (Figs. 3 and 5). In contrast, during high-flow samplings (III, IV, and V), As remained predominantly associated with the particulate fraction at both high and low tides. During high-flow conditions, the predominance of As in the particulate fraction is consistent with inputs coming from upstream reaches, where Fe minerals already carrying adsorbed As are transported into the estuary. This interpretation aligns with observations of Papaslioti et al. (2024), who reported that post-rainfall events enhance the transport of As bound to Fe-rich particles from the Tinto River. In sampling IV, the "on–off" pattern reappeared under flood tides with pH values above 6, resulting in a measurable increase in the dissolved fraction.

The "on–off" behaviour of As likely reflects sorption–desorption dynamics controlled by As speciation and the stability and surface properties of newly-formed Fe precipitates, mainly schwertmannite (e.g., Carrero et al., 2015; Alarcón et al., 2014; Antelo et al., 2021; Paikaray, 2021; Schoepfer & Burton, 2021; Park et al., 2023; Pérez-López et al., 2023). The arsenic speciation derived from PHREEQC modelling in this study indicates a predominance of As(V) oxyanions ($H_2AsO_4^-$ and $HAsO_4^{2-}$) for the entire pH range. Under acidic conditions, schwertmannite exhibits a positive surface charge, thereby elucidating its pronounced affinity for As. However, when the pH exceeds the schwertmannite point of zero charge (PZC) (approximately between pH 6 and 7; Burton et al., 2009; Antelo et al., 2012; Carrero et al., 2017; Shi et al., 2021), the sorption sites become negatively charged, which generates electrostatic repulsion with the previously adsorbed As species ("on") and causes its desorption ("off"). Consequently, this suggests that almost the total concentration of As coming from the Tinto River is ultimately discharged into the Atlantic Ocean together with the conservative elements.

3.4. *Suspended particulate matter (SPM)*

FESEM-EDX analyses revealed distinct variations in the SPM composition between different tidal coefficients and under varying discharge conditions. Under low-flow (I and II), ebb tide samples were dominated by Fe oxyhydroxisulfates, occasionally with traces of sorbed (hereafter used as a general term including adsorption and co-precipitation processes) Pb and As (Fig. SM7A). Among these phases, a mineral phase with the characteristic "pin-cushion" morphology and composition typical of schwertmannite was observed (Fig. SM7B), consistent with PHREEQC results (Table SM6 and Fig. SM6). On the other hand, samples collected during flood tides contained preferentially Al precipitates occasionally associated with Cu, which probably correspond to basaluminite (Fig. 6A), also in agreement with the modelled SI calculations. Additionally, flood tide samples contained abundant marine microorganisms, comprising centric and pennate diatoms, along with rod-shaped bacterial forms embedded within mineral aggregates (Fig. SM7C-E). In contrast, high-flow campaigns (III, IV, V) were characterized by abundant Fe minerals, likely schwertmannite, which sorbed Pb and As throughout the tidal cycles (Fig. 6B-C and SM7F-G). Compared to Fe, Al minerals were scarce whereas barite and detrital components, including clays and aluminium silicates, were abundant. No evidence of marine microorganisms, like diatoms, was detected under high-flow conditions.

The SPM concentration in the analysed samples is represented in Fig. 7. Maximum concentrations are reached during ebb tides, when fluvial influence dominates, and then decrease abruptly during the early stages of the flood tide. During the subsequent tidal rise, SPM concentrations show a slight increase with SWf, suggesting in situ precipitation during estuarine mixing, sediment resuspension and/or tidal advection of particulate material toward the sampling site (Verney et al., 2024). These patterns indicate that SPM fluctuations are modulated by the tidal stages and reflect the interplay between physical transport from upstream areas and spatial trends in mineral precipitation during the mixing process (Zhang et al., 2015).

The bulk composition of SPM is shown in Table 3. The SPM is primarily composed of Fe and Al, as expected by their previously discussed hidrogeochemical behaviour. The remaining elements follow the relative abundance order: Cu > Pb > As > Zn > Mn > Ni > Co > Cd. Across the three sampling campaigns, particulate concentrations show clear relationships with the physicochemical gradients, with broadly consistent patterns in campaigns III and V (Table SM8). In both campaigns,

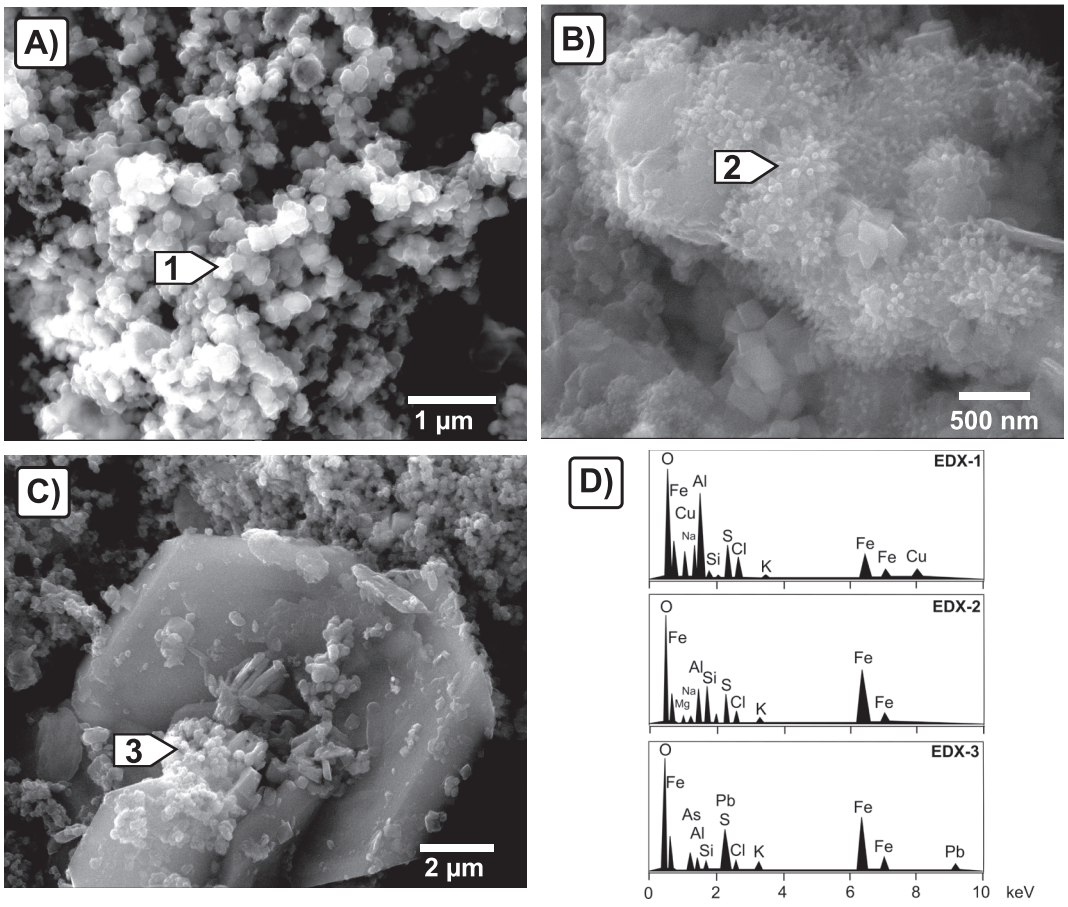

Fig. 6. Representative FESEM images of SPM: (A) basaluminite-like particles with sorbed Cu in sample I-14, (B) schwertmannite-like "pin-cushion" aggregates in sample IV-22, (C) schwertmannite-like particles with sorbed As and Pb in sample III-7, and (D) selected EDX spectra of points of interest.

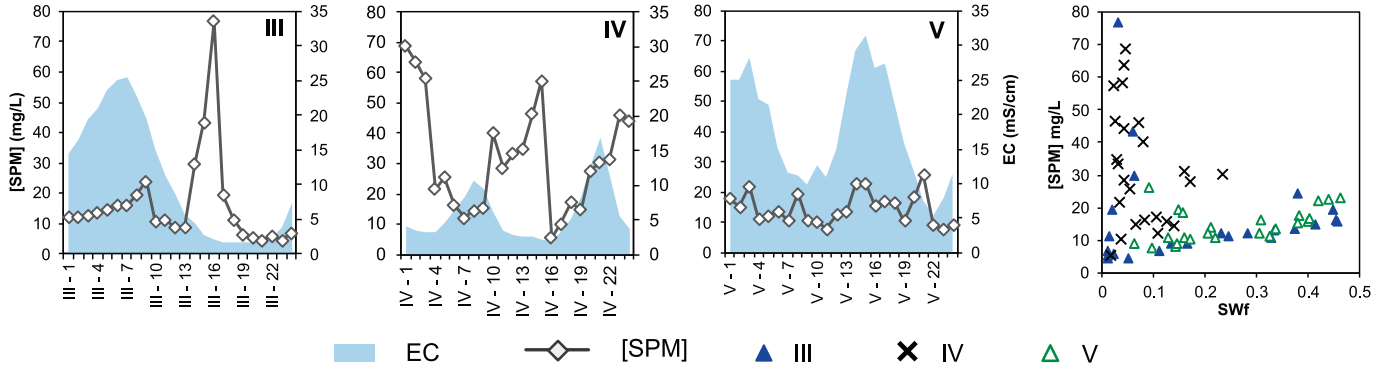

Fig. 7. Suspended particulate matter (SPM) concentration evolution during tidal cycles and with SWf for sampling campaigns III, IV, and V.

most metal(oid)s (e.g., Fe, Mn, Co, Cd, As, Pb) display strong negative correlations with pH, EC, and SWf, along with positive relationship with Eh, whereas Al and Cu exhibit the opposite pattern. These results support the interpretations outlined in the previous section concerning the sequential precipitation of Fe and Al. As pH rises during early stages of riverwater–seawater mixing upstream, prior Fe precipitation occurs, which scavenges other contaminants. These Fe-rich precipitates likely sedimentate before reaching the sampling point, thus reducing their concentrations in the SPM as the marine influence increases downstream. Whereas Al and Cu become incorporated into the SPM under more advanced mixing conditions downstream in samplings III and V, patterns in campaign IV are more variable, exhibiting weaker and sometimes even opposite correlations for elements such as Al, Zn or Cu.

Iron, Al, Pb and Cu consistently exhibited the highest Kd values (Table 4), confirming their strong partitioning into the particulate phase. Conversely, Zn, Mn, Co, Ni and Cd showed relatively lower Kd values, indicating a greater tendency to remain in the dissolved phase, except in sampling IV where comparably higher values were observed (Table 4). A plausible explanation is that the low seawater influence during sampling IV (i.e., SWf < 0.3 across all samples, Fig. 3) resulted in reduced ionic strength and lower concentrations of competing cations such as Na^{+}, Ca^{2+}, and Mg^{2+}. Consequently, the decreased competition for reactive sorption sites on Fe and Al oxyhydroxides likely enhanced the affinity of these phases for trace metal adsorption (Achterberg et al., 2003; Duc et al., 2013). Arsenic showed the greatest variability, with high and low values (Table 4), possibly associated to its "on–off"

Table 3
Suspended particulate matter (SPM) concentration of selected samples in mass per unit.

Sample	pH	Fe mg/g	Al	Cu µg/g	Pb	As	Zn	Mn	Co	Ni	Cd	Ba
III-6	4.70	97.8	37.1	644	1078	<d.l.	202	60.2	3.18	5.59	0.35	122
III-12	3.37	160	8.01	340	1413	<d.l.	265	142	8.01	6.94	0.97	329
III-14	3.23	157	10.9	443	2452	<d.l.	343	157	9.00	13.14	0.78	631
III-16	3.20	162	10.6	420	2401	1297	204	151	8.23	9.49	0.73	647
III-22	3.20	229	9.86	455	1186	765	102	157	9.80	<d.l.	1.73	246
IV-2	4.88	89.0	34.0	2250	851	460	488	161	10.7	17.13	1.30	202
IV-9	6.28	84.5	20.2	1633	724	470	1158	140	12.5	4.49	2.48	112
IV-12	4.90	97.7	30.3	1509	814	409	314	153	8.92	12.76	1.05	224
IV-16	4.18	79.4	17.3	867	753	358	161	158	11.4	39.65	1.81	138
IV-23	5.55	89.0	28.5	1367	779	428	319	112	7.59	8.67	0.82	234
V-3	5.12	68.8	90.2	967	83.2	<d.l.	152	15.7	1.47	3.29	0.21	4.76
V-9	3.22	498	9.21	448	164	<d.l.	236	103	5.91	1.61	0.76	32.9
V-14	4.84	97.5	125	1518	129	<d.l.	226	32.1	1.87	2.33	0.31	11.0
V-16	4.74	94.1	40.2	698	101	<d.l.	72.8	24.6	1.58	<d.l.	0.29	19.5
V-21	3.20	277	9.07	379	146	<d.l.	120	66.0	3.58	2.66	0.39	30.8

Table 4
Partition coefficients of metals (Kd, L/kg) range in estuarine samples from sampling campaigns III, IV, and V (mean; median). Kd values could not be calculated when particulate concentrations were below the detection limit and are therefore reported as < d.l.

(L/kg)	III		IV		V	
Kd Li	<d.l. - 328	(251; —)	419–728	(520; 470)	(520; 470)	—
Kd Al	480–10471	(2518; 542)	1651–454329	(96864; 10411)	330–53643	(22786; 7509)
Kd Mn	80.1–60207	(12112; 88.0)	133–306	(186; 163)	15.5–46.4	(27.8; 25.2)
Kd Fe	5056–16089	(8017; 6686)	6343–14035831	(2817317; 15370)	14957–60193	(40493;40506)
Kd Co	62.2–91.3	(79.6–84.0)	184–645	(296; 190)	23.3–44.6	(30.3; 26.2)
Kd Ni	<d.l.-475	(373; 352)	598–2419	(1143; 904)	<d.l.-230	(134; 127)
Kd Cu	120–620	(230; 139)	433–93223	(19927;1731)	73.8–999	(459; 384)
Kd Zn	12.9–93.4	(46.8;50.0)	42.2–1822	(469; 146)	14.8–93.9	(46.3; 32.9)
Kd As	0.40–458138	(149601; 0.80)	46822–342068	(154091; 137076)	0.66–1.67	(1.27; 1.32)
Kd Cd	1.66–4.35	(2.89; 3.09)	42.4–4773	(1001; 67.7)	5.91–24.4	(15.8; 17.3)
Kd Ba	6101–29749	(18154; 15412)	8518–15580	(12153; 12605)	281–1995	(1189; 1214)
Kd Pb	2988–10916	(5925; 5443)	19637–1394038	(312560; 44449)	2220–9982	(5660; 6079)

behaviour.

In general, Kd values (Table SM8) increased with pH, EC and SWf for most elements analyzed, indicating a greater affinity for the particulate phase under more marine conditions. Nickel, Co, Mn, and As deviate from this general behaviour, showing markedly different correlation patterns depending on the hydrological context. These exceptions likely reflect the more complex speciation, sorption behaviour, redox sensitivity or dependence on other factors (e.g., ionic competition, organic matter and SPM particle size) for these elements, which can lead to distinct partitioning mechanisms under varying estuarine mixing conditions (Eliott et al., 2011; de Caravalho et al., 2021; Ferreira et al., 2024).

4. Environmental implications

To quantify the contaminants that were exported from the Tinto River to the estuary and ultimately to the ocean, dissolved metal(loid)s loads were estimated for the five sampling campaigns following the methodology described by Olías et al. (2006). Estimated loads were then compared with the average values reported for the 1995–2003 and 2017–2018 periods (see Table 5; Olías et al., 2006, 2020). The dissolved loads transported by the Tinto River show marked variability associated with the hydrological regime. Daily loads calculated for high-flow episodes (samples III–V) exceed the daily averages reported by Olías et al. (2006, 2020) for the 1995–2003 and 2017–2018 periods. For instance, the maximum values recorded in this study for Fe (87.6 t/day), SO_4^{2-} (754.6 t/day) and Zn (10.1 t/day) are several times higher than the historical averages. This fact confirms that flood events represent the periods of maximum gross export of pollutants, highlighting the necessity for targeted monitoring under these conditions.

The partitioning patterns observed indicate that non-conservative elements such as Fe, Al, Cu, and Pb have a marked tendency to be

Table 5
Calculated Tinto River dissolved loads from this study and average of 1995–2003 and 2017–2018 periods.

	SO_4	Fe	Al	Mn	Cu	Zn	Co	Ni	As	Cd	Pb
	t/day						kg/day				
I (low flow)	0.17–1.51	0.02–0.16	0.01–0.09	0.00–0.01	0.00–0.02	0.00–0.02	0.06–0.52	0.01–0.11	0.00–0.03	0.01–0.07	0.00–0.03
II (low flow)	0.19–1.72	0.02–0.14	0.01–0.09	0.00–0.01	0.00–0.02	0.00–0.02	0.07–0.61	0.01–0.13	0.00–0.02	0.01–0.07	0.00–0.03
III (high flow)	507–755	58.8–87.5	22.4–33.3	2.60–3.87	5.61–8.35	6.81–10.1	177–263	30.1–44.8	7.16–10.6	27.4–40.8	218–324
IV (high flow)	378–863	27.2–62.0	16.5–37.6	1.69–3.85	3.30–7.51	3.70–8.44	108–247	26.4–60.4	2.23–5.10	15.8–36.1	61.5–140
V (high flow)	370–539	27.2–39.6	19.5–28-4	1.72–2.51	3.79–5.52	3.79–5.52	121–176	22.1–32.2	1.50–2.19	16.6.24.2	23.3–34.0
1995–2003 (Olías et al., 2006)	100	13.9	3.35	0.45	1.28	2.36	23.8	6.03	34.0	10.7	40.5
2017–2018 (Olías et al., 2020)	135	13.6	7.11	0.64	1.52	1.87	41.1	8.22	9.86	5.75	41.1

incorporated into suspended particulate matter as marine influence increases. This process reduces their effective export to coastal waters while favouring their accumulation in estuarine sediments. The net flux to the ocean may decrease by up to 100% for Fe, Al, and Pb, as suggested by their dissolved fractions (%D) and Kd values during seawater mixing, which point to near-complete retention within the estuary. In contrast, the reduction in Cu flux is expected to be more limited since, under high seawater fractions, a portion of dissolved Cu can form stable chloride complexes and behave quasi-conservatively.

In contrast, elements with more conservative behaviour – namely, Mn, Co, Ni, Zn, and Cd – show limited retention in SPM within the pH range recorded in this study. Consequently, a substantial portion of their loads may be transported directly to the Atlantic Ocean or undergo partial attenuation and accumulate in the outer estuary, where pH values exceed 7.5 and can favour their incorporation into sediments. Arsenic, displaying its characteristic "on–off" behaviour, is expected to be exported mainly during high tide through desorption from schwertmannite, implying that the dissolved load delivered by the river approximates the effective net flux to the ocean.

Additionally, high river flow conditions may also potentially enhance the transport and deposition of metal-rich particles in the middle and outer areas of the estuary, while low-flow conditions would favour their accumulation in the upper estuary (Coates-Marnane et al., 2016). This accumulation poses a potential long-term risk, as remobilisation may occur under changing redox or pH conditions, or even anthropogenic activities. In this sense, the port of Huelva, located in the outer estuary, carries out periodic dredging to condition the channel for cargo ships. If metal-rich sediments indeed reach the estuary channel, their dredge-induce remobilization may potentially cause sudden changes in equilibrium conditions which could end up releasing metalloids back into the aquatic environment and even into the ocean, posing great concerns for the environmental management of the outer estuary section (Sánchez-Moyano et al., 2025). Further research should aim at in-dept characterization of sediment transport processes in the Ría de Huelva Estuary (e.g., turbidity spatial profiles and its relationship with metal-rich SPM).

The results obtained provide an unprecedented level of detail in assessing the dynamics of AMD-derived contaminants in the Tinto River estuary and their potential transfer to the Atlantic Ocean. The fixed-station, high-temporal-resolution sampling strategy employed proves to be a valuable tool for highly variable systems such as AMD-impacted estuaries, where diurnal and fortnightly tidal cycles induce abrupt fluctuations in pH, conductivity and elemental composition. These abrupt fluctuations may have a significant increase of pollutant exposure to aquatic organisms, leading to bioaccumulation of metals along the trophic chain.

Unlike spatial sampling, which relies on boat-based surveys and is constrained by tidal windows and estuarine navigability, fixed-station sampling captures the full transition from low to high tide without interruption. This approach ensures an accurate characterization of phase transitions (dissolved–particulate), pollution pulses and sorption processes that occur during estuarine mixing. This strategy is particularly advantageous for characterising short-lived but environmentally significant events, such as floods, storms, or one-off discharges, that often go undetected in conventional monitoring programmes. The main limitation is the restricted range of seawater fractions recorded: under low-flow conditions, SWf values range between 0.5 and 1.0, whereas under high-flow conditions SWf values are predominantly below 0.5. Nevertheless, this constraint does not compromise the interpretation of the underlying processes, as daily tidal variations are fully captured, allowing each phase of the tidal cycle to be accurately linked to the sampling events and the resulting geochemical response.

5. Conclusions

This study provides the first tide-resolved and hydrologically contrasted characterization of metal(loid) dynamics in the AMD-impacted Tinto River estuary, demonstrating that element-specific geochemical behaviour is controlled by the interaction between tidal forcing and river discharge, which modulates physicochemical gradients, mineral precipitation, and particulate–dissolved partitioning, ultimately governing contaminant retention and export. The high-frequency sampling approach further resolves variability at daily and fortnightly tidal scales, advancing the understanding of estuarine geochemical functioning.

Across all campaigns, daily tidal cycles induced sharp fluctuations in physicochemical parameters and dissolved metal(oid)s concentrations. Low tides consistently recorded peaks in dissolved contaminants due to the dominance of acidic fluvial water, whereas flood tides, and associated pH increases, enhanced the transfer of non-conservative metal(oid)s (i.e., Fe, Al, Cu, As, and Pb) to the particulate phase, mainly schwertmannite and basaluminite, thereby reducing their mobility and bioavailability. However, quasi-conservative elements (i.e., Zn, Mn, Co, Ni and Cd) have a minimal participation in sorption processes in the recorded physicochemical conditions, thus being efficiently net-transported to the coast.

Arsenic, previously sorbed onto schwertmannite under more acidic conditions, is desorbed when pH exceeds 6 due to electrostatic repulsion above the mineral's point of zero charge, underscoring a significant risk of enhanced As net flux to coastal waters. Lead also displayed a singular behaviour, with unusually high dissolved concentrations under specific high-flow conditions, likely governed by sulfate-mineral solubility control (e.g., anglesite or jarosite). Given its toxicity, this response warrants further investigation.

The mineralogical and geochemical evidence (FESEM observations and PHREEQC modelling) suggest the sequential precipitation of schwertmannite followed by basaluminite, a process that shapes the composition of SPM. The SPM seems to form primarily during early estuarine mixing, when initial pH increases trigger rapid precipitation; subsequently transported and locally regenerated through in situ precipitation and/or sediment resuspension. This sequence provides a mechanistic framework for understanding particulate formation and transformation in acidic estuarine environments.

Some limitations should be acknowledged. The fixed-station sampling design does not resolve the full estuarine mixing gradient, and the dataset is biased towards marine-dominated conditions during low-flow and fluvial-dominated conditions during high-flow. Future studies could address this limitation by combining fixed-point monitoring with simultaneous upstream and downstream sampling stations to capture the complete salinity gradient.

Notwithstanding these constraints, this study provides a process-based framework that is broadly applicable to other AMD-impacted estuarine systems worldwide. The identified geochemical processes and their coupling with tidal and hydrological dynamics offer a baseline for evaluating how climate-driven changes (e.g., sea level rise, hydrological variability), accidental pollutant spills (e.g. mine/industrial tailings rupture), and promising anthropogenic interventions at contaminant sources (e.g., mining remediation, industrial wate restoration) may alter estuarine mixing and pollutant export to coastal waters.

CRediT authorship contribution statement

Laura Sánchez-López: Writing – review & editing, Writing – original draft, Visualization, Methodology, Data curation, Conceptualization. **Jonatan Romero-Matos:** Writing – review & editing, Methodology, Data curation. **Carlos R. Cánovas:** Writing – review & editing, Supervision, Investigation, Funding acquisition, Conceptualization. **Rémi Freydier:** Writing – review & editing, Methodology. **Rafael Pérez-López:** Writing – review & editing, Supervision, Project administration, Funding acquisition, Conceptualization.

Declaration of competing interest

The authors declare that they have no known competing financial interests or personal relationships that could have appeared to influence the work reported in this paper.

Acknowledgements

This work was supported by the Spanish Ministry of Science, Innovation and Universities under the research project DYNAMICO (PID2023-151504OB-I00) funded by MICIU/AEI/10.13039/501100011033. J. Romero-Matos is financed by a FPU program of the Spanish Ministry of Education and Vocational Training (FPU20/04441). L. Sánchez-López acknowledges the "Formación de Personal Investigador" grant (PRE2021-097651) funded by MCIN/AEI/10.13039/501100011033. Additional information may be obtained by contacting the corresponding author. The authors sincerely thank the Ayuntamiento de San Juan del Puerto and the staff of the Centro Municipal de Actividades Náuticas, especially Rafael and Miguel, for their support in site access and field sampling logistics. The authors gratefully appreciate the constructive comments and suggestions from the associate editor and two anonymous reviewers, which greatly contributed to improving the manuscript. Funding for open access charge: Universidad de Huelva/CBUA.

Appendix A. Supplementary data

Supplementary data to this article can be found online at https://doi.org/10.1016/j.jhydrol.2026.135799.

Data availability

Data will be made available on request.

References

Abdou, M., Tercier-Waeber, M.L., Dutruch, L., Bossy, C., Pougnet, F., Coynel, A., Bakker, E., Blanc, G., Schäfer, J., 2022. Estuarine dissolved speciation and partitioning of trace metals: a novel approach to study biogeochemical processes. Environ. Res. 208, 112596. https://doi.org/10.1016/j.envres.2021.112596.

Acero, P., Ayora, C., Torrentó, C., Nieto, J.M., 2006. The behavior of trace elements during schwertmannite precipitation and subsequent transformation into goethite and jarosite. Geochim. Cosmochim. Acta 70 (16), 4130–4139. https://doi.org/10.1016/j.gca.2006.06.1367.

Achterberg, E.P., Herzl, V.M.C., Braungardt, C.B., Millward, G.E., 2003. Metal behaviour in an estuary polluted by acid mine drainage: the role of particulate matter. Environ. Pollut. 121 (2), 283–292. https://doi.org/10.1016/S0269-7491(02)00216-6.

Alarcón, R., Gaviria, J., Dold, B., 2014. Liberation of adsorbed and co-precipitated arsenic from jarosite, schwertmannite, ferrihydrite, and goethite in seawater. Minerals 4 (3), 603–620. https://doi.org/10.3390/min4030603.

Antelo, J., Fiol, S., Gondar, D., López, R., Arce, F., 2012. Comparison of arsenate, chromate and molybdate binding on schwertmannite: surface adsorption vs anion-exchange. J. Colloid Interface Sci. 386 (1), 338–343. https://doi.org/10.1016/j.jcis.2012.07.008.

Antelo, J., Fiol, S., Carabante, I., Arroyo, A., Lezama-Pacheco, J.S., Josevska, N., Protopapa, C., Kumpiene, J., 2021. Stability of naturally occurring AMD–schwertmannite in the presence of arsenic and reducing agents. J. Geochem. Explor. 220, 106677. https://doi.org/10.1016/j.gexplo.2020.106677.

Asta, M.P., Ayora, C., Román-Ross, G., Cama, J., Acero, P., Gault, A.G., Charnock, J.M., Bardelli, F., 2010. Natural attenuation of arsenic in the Tinto Santa Rosa acid stream (Iberian Pyritic Belt, SW Spain): the role of iron precipitates. Chem. Geol. 271 (1–2), 1–12. https://doi.org/10.1016/j.chemgeo.2009.12.005.

Asta, M.P., Calleja, M.L., Pérez-López, R., Auqué, L.F., 2015. Major hydrogeochemical processes in an acid mine drainage affected estuary. Mar. Pollut. Bull. 91 (1), 295–305. https://doi.org/10.1016/j.marpolbul.2014.11.023.

Augustinus, P., Barton, C.E., Zawadzki, A., Harle, K., 2010. Lithological and geochemical record of mining-induced changes in sediments from Macquarie Harbour, southwest Tasmania Australia. Environ. Earth Sci. 61 (3), 625–639. https://doi.org/10.1007/s12665-009-0377-x.

Ball, J. W., & Nordstrom, D. K. (1991). User's manual for WATEQ4F, with revised thermodynamic data base and test cases for calculating speciation of major, trace, and redox elements in natural waters (U.S. Geological Survey Open-File Report 91–183). U.S. Geological Survey. doi: 10.3133/ofr91183.

Basallote, M.D., Cánovas, C.R., Olías, M., Pérez-López, R., Macías, F., Carrero, S., Ayora, C., Nieto, J.M., 2019. Mineralogically-induced metal partitioning during the evaporative precipitation of efflorescent sulfate salts from acid mine drainage. Chem. Geol. 530, 119339. https://doi.org/10.1016/j.chemgeo.2019.119339.

Blanc, P., Lassin, A., Piantone, P., Azaroual, M., Jacquemet, N., Fabbri, A., Gaucher, E.C., 2012. Thermoddem: a geochemical database focused on low temperature water/rock interactions and waste materials. Appl. Geochem. 27 (10), 2107–2116. https://doi.org/10.1016/j.apgeochem.2012.06.002.

Borrego, J., López-González, N., Carro, B., 2004. Geochemical signature as paleoenvironmental markers in Holocene sediments of the Tinto River estuary (Southwestern Spain). *Estuarine*. Coastal Shelf Sci. 61 (4), 631–641. https://doi.org/10.1016/j.ecss.2004.07.004.

Braungardt, C.B., Achterberg, E.P., Elbaz-Poulichet, F., Morley, N.H., 2003. Metal geochemistry in a mine-polluted estuarine system in Spain. Appl. Geochem. 18 (11), 1757–1771. https://doi.org/10.1016/S0883-2927(03)00079-9.

Braungardt, C.B., Howell, K.A., Tappin, A.D., Achterberg, E.P., 2011. Temporal variability in dynamic and colloidal metal fractions determined by high resolution in situ measurements in a UK estuary. Chemosphere 84, 423–431. https://doi.org/10.1016/j.chemosphere.2011.03.050.

Burton, E.D., Bush, R.T., Johnston, S.G., Watling, K.M., Hocking, R.K., Sullivan, L.A., Parker, G.K., 2009. Sorption of arsenic (V) and arsenic (III) to schwertmannite. Environ. Sci. Technol. 43 (24), 9202–9207. https://doi.org/10.1021/es902461x.

Cánovas, C.R., Olías, M., Nieto, J.M., Sarmiento, A.M., Cerón, J.C., 2007. Hydrogeochemical characteristics of the Tinto and Odiel Rivers (SW Spain). factors controlling metal contents. Sci. Total Environ. 373 (1), 363–382. https://doi.org/10.1016/j.scitotenv.2006.11.022.

Cánovas, C.R., Hubbard, C.G., Olías, M., Nieto, J.M., Black, S., Coleman, M.L., 2008. Hydrochemical variations and contaminant load in the Río Tinto (Spain) during flood events. J. Hydrol. 350 (1–2), 25–40. https://doi.org/10.1016/j.jhydrol.2007.11.022.

Cánovas, C.R., Olías, M., Nieto, J.M., Galván, L., 2010. Wash-out processes of evaporitic sulfate salts in the Tinto river: hydrogeochemical evolution and environmental impact. Appl. Geochem. 25 (2), 288–301. https://doi.org/10.1016/j.apgeochem.2009.11.014.

Cánovas, C.R., Olías, M., Vázquez-Suñé, E., Ayora, C., Nieto, J.M., 2012. Influence of releases from a fresh water reservoir on the hydrochemistry of the Tinto River (SW Spain). Sci. Total Environ. 416, 418–428. https://doi.org/10.1016/j.scitotenv.2011.11.079.

Carlson, L., Bigham, J.M., Schwertmann, U., Kyek, A., Wagner, F., 2002. Scavenging of as from acid mine drainage by schwertmannite and ferrihydrite: a comparison with synthetic analogues. Environ. Sci. Technol. 36 (8), 1712–1719. https://doi.org/10.1021/es0110271.

Carrera, J., Vázquez-Suñé, E., Castillo, O., Sánchez-Vila, X., 2004. A methodology to compute mixing ratios with uncertain end-members. Water Resour. Res. 40 (12), 1–11. https://doi.org/10.1029/2003WR002263.

Carrero, S., Pérez-López, R., Fernandez-Martinez, A., Cruz-Hernández, P., Ayora, C., Poulain, A., 2015. The potential role of aluminium hydroxysulphates in the removal of contaminants in acid mine drainage. Chem. Geol. 417, 414–423. https://doi.org/10.1016/j.chemgeo.2015.10.020.

Carrero, S., Fernandez-Martinez, A., Pérez-López, R., Poulain, A., Salas-Colera, E., Nieto, J.M., 2017. Arsenate and selenate scavenging by basaluminite: insights into the reactivity of aluminum phases in acid mine drainage. Environ. Sci. Tech. 51 (1), 28–37. https://doi.org/10.1021/acs.est.6b03315.

Cereja, R., Brotas, V., Nunes, S., Rodrigues, M., Cruz, J.P.C., Brito, A.C., 2022. Tidal influence on water quality indicators in a temperate mesotidal estuary (Tagus Estuary, Portugal). Ecol. Ind. 136, 108715. https://doi.org/10.1016/j.ecolind.2022.108715.

Coates-Marnane, J., Olley, J., Burton, J., Grinham, A., 2016. The impact of a high magnitude flood on metal pollution in a shallow subtropical estuarine embayment. Sci. Total Environ. 569–570, 716–731. https://doi.org/10.1016/j.scitotenv.2016.06.193.

Consani, S., Ianni, M.C., Cutroneo, L., Dinelli, E., Carbone, C., Capello, M., 2019. Environmental implications of metal mobility in marine sediments receiving input from a torrent affected by mine discharge. Mar. Pollut. Bull. 139, 221–230. https://doi.org/10.1016/j.marpolbul.2018.12.050.

Davis, J.C., 2002. Statistics and Data Analysis in Geology. John Wiley & Sons, USA.

Davis, R.A., Welty, A.T., Borrego, J., Morales, J.A., Pendon, J.G., Ryan, J.G., 2000. Rio Tinto estuary (Spain): 5000 Years of pollution. Environ. Geol. 39 (10), 1107–1116. https://doi.org/10.1007/s002549900096.

Dean, A.P., Lynch, S., Rowland, P., Toft, B.D., Pittman, J.K., White, K.N., 2013. Natural wetlands are efficient at providing long-term metal remediation of freshwater systems polluted by acid mine drainage. Environ. Sci. Technol. 47 (21), 12029–12036. https://doi.org/10.1021/es4025904.

De Caravalho, L.M., Hollister, A.P., Trindade, C., Gledhill, M., Koschinsky, A., 2021. Distribution and size fractionation of nickel and cobalt species along the Amazon estuary and mixing plume. Mar. Chem. 236, 104019. https://doi.org/10.1016/j.marchem.2021.104019.

de Souza Machado, A.A., Spencer, K., Kloas, W., Toffolon, M., Zarfl, C., 2016. Metal fate and effects in estuaries: a review and conceptual model for better understanding of toxicity. Sci. Total Environ. 541, 268–281. https://doi.org/10.1016/j.scitotenv.2015.09.045.

Duc, T.A., Loi, V.D., Thao, T.T., 2013. Partition of heavy metals in a tropical river system impacted by municipal waste. Environmental Monitoring Assessment 185, 1907–1925. https://doi.org/10.1007/s10661-012-2676-z.

Elbaz-Poulichet, F., Morley, N.H., Cruzado, A., Velasquez, Z., Achterberg, E.P., Braungardt, C.B., 1999. Trace metal and nutrient distribution in an extremely low pH (2.5) river–estuarine system, the Ría of Huelva (South-West Spain). Sci. Total Environ. 227 (1–2), 73–83. https://doi.org/10.1016/S0048-9697(99)00006-6.

Eliott, A.V.C., Plach, J.M., Droppo, I.G., Warren, L.A., 2011. Comparative floc-bed sediment trace element partitioning across variably contaminated aquatic ecosystems. Environ. Sci. Tech. 46 (1), 209–216. https://doi.org/10.1021/es202221u.

Ferreira, A.D., Duckworth, O.W., Queiroz, H.M., Nóbrega, G.N., Barcellos, D., Bernardino, Â.F., Otero, X.L., Ferreira, T.O., 2024. Seasonal drives on potentially toxic elements dynamics in a tropical estuary impacted by mine tailings. J. Hazard. Mater. 474, 134592. https://doi.org/10.1016/j.jhazmat.2024.134592.

Fukushi, K., Sasaki, M., Sato, T., Yanase, N., Amano, H., 2003. A natural attenuation of arsenic in drainage from an abandoned arsenic mine dump. Appl. Geochem. 18 (8), 1267–1278. https://doi.org/10.1016/S0883-2927(03)00011-8.

Garbarino, J.R., Hoffman, G.L., 1999. Methods of Analysis by the U.S. Geological Survey National Water Quality Laboratory, Comparison of a Nitric Acid in-Bottle Digestion Procedure to Other Whole-Water Digestion Procedures. In: Open File Rep, 99–094. U.S. Geological Survey, Denver, Colorado. https://doi.org/10.3133/ofr9994.

Hadikhani, R., Karbassi, A., Tajziehchi, S., Mehdizadeh, Y., 2024. Mechanisms and controlling factors of heavy metals removal by electroflocculation in estuarine environments. Mar. Pollut. Bull. 206, 116699. https://doi.org/10.1016/j.marpolbul.2024.116699.

Harris, D.L., Lottermoser, B.G., Duchesne, J., 2003. Ephemeral acid mine drainage at the Montalbion silver mine, north Queensland. Aust. J. Earth Sci. 50 (5), 797–809. https://doi.org/10.1111/j.1440-0952.2003.01029.x.

Heidari, M., 2019. Role of natural flocculation in eliminating toxic metals. Arch. Environ. Contam. Toxicol. 76 (3), 366–374. https://doi.org/10.1007/s00244-019-00597-x.

Hierro, A., Olías, M., Cánovas, C.R., Martín, J.E., Bolivar, J.P., 2014a. Trace metal partitioning over a tidal cycle in an estuary affected by acid mine drainage (Tinto estuary, SW Spain). Sci. Total Environ. 497–498, 18–28. https://doi.org/10.1016/j.scitotenv.2014.07.070.

Hierro, A., Olías, M., Ketterer, M.E., Vaca, F., Borrego, J., Cánovas, C.R., Bolivar, J.P., 2014b. Geochemical behavior of metals and metalloids in an estuary affected by acid mine drainage (AMD). Environ. Sci. Pollut. Res. 21 (4), 2611–2627. https://doi.org/10.1007/s11356-013-2189-5.

Jennings, E., Onnis, P., Crane, R., Comber, S.D.W., Byrne, P., Riley, A.L., Mayes, W.M., Jarvis, A.P., Hudson-Edwards, K.A., 2025. Spatial and temporal (annual and decadal) trends of metal(loid) concentrations and loads in an acid mine drainage-affected river. Sci. Total Environ. 964 (2), 178496. https://doi.org/10.1016/j.scitotenv.2025.178496.

Jung, H.B., Yun, S.T., Kwon, J.S., Zheng, Y., 2012. Role of iron colloids in copper speciation during neutralization in a coastal acid mine drainage, South Korea: insight from voltammetric analyses and surface complexation modeling. J. Geochem. Explor. 112, 244–251. https://doi.org/10.1016/j.gexplo.2011.09.002.

Leblanc, M., Morales, J.A., Borrego, J., Elbaz-Poulichet, F., 2000. 4,500-year-old mining pollution in southwestern Spain: long-term implications for modern mining pollution. Econ. Geol. 95 (3), 655–661. https://doi.org/10.2113/gsecongeo.95.3.655.

Li, B., Liu, G., Nie, Y., Ye, Z., 2021. Causes and Effects of a Water Spill from the Underground Pit of the Dashu Pyrite Mine, Southern Sichuan Basin, Southwest China. Mine Water Environ. 40 (4), 864–876. https://doi.org/10.1007/s10230-021-00825-8.

Lozano, A., Ayora, C., Macías, F., León, R., Gimeno, M.J., Auqué, L., 2020. Geochemical behavior of rare earth elements in acid drainages: modeling achievements and limitations. J. Geochem. Explor. 216. https://doi.org/10.1016/j.gexplo.2020.106577.

Millán-Becerro, R., Pérez-López, R., Cánovas, C.R., Macías, F., León, R., 2023. Phosphogypsum weathering and implications for pollutant discharge into an estuary. J. Hydrol. 617, 128943. https://doi.org/10.1016/j.jhydrol.2022.128943.

Montecinos, M., Briso, A., Vega, A., Pastén, P., 2022. Settling of copper-rich suspended particles from acid drainage neutralization as a function of chemical composition and particle size distribution. Appl. Geochem. 142, 105271. https://doi.org/10.1016/j.apgeochem.2022.105271.

Moreno-González, R., Macías, F., Olías, M., Ruiz Cánovas, C., 2022. Temporal evolution of acid mine drainage (AMD) leachates from the abandoned tharsis mine (Iberian Pyrite Belt, Spain). Environ. Pollut. 295, 118697. https://doi.org/10.1016/j.envpol.2021.118697.

Nascimento, Â., Biguino, B., Borges, C., Cereja, R., Cruz, J.P.C., Sousa, F., Dias, J., Brotas, V., Palma, C., Brito, A.C., 2021. Tidal variability of water quality parameters in a mesotidal estuary (Sado Estuary, Portugal). Sci. Rep. 11 (1), 1–17. https://doi.org/10.1038/s41598-021-02603-6.

Nascimento, S.C., Cooke, D.R., Townsend, A.T., Davidson, G., Parbhakar-Fox, A., Cracknell, M.J., Miller, C.B., 2023. Long-term impact of historical mining on water quality at mount lyell, Western Tasmania, Australia. Mine Water Environ. 42, 399–417. https://doi.org/10.1007/s10230-023-00943-5.

Nieto, J.M., Sarmiento, A.M., Canovas, C.R., Olias, M., Ayora, C., 2013. Acid mine drainage in the Iberian Pyrite Belt: 1. hydrochemical characteristics and pollutant load of the Tinto and Odiel rivers. Environ. Sci. Pollut. Res. 20 (11), 7509–7519. https://doi.org/10.1007/s11356-013-1634-9.

Nordstrom, D.K., 2011. Hydrogeochemical processes governing the origin, transport and fate of major and trace elements from mine wastes and mineralized rock to surface waters. Appl. Geochem. 26 (11), 1777–1791. https://doi.org/10.1016/j.apgeochem.2011.06.002.

Nordstrom, D.K., Wilde, F.D., 1998. Reduction–oxidation potential (electrode method). national field manual for the collection ofwater quality data. U.S. geological survey techniques of water-resources investigations. Book 9, 6.5.

Olías, M., Cánovas, C.R., Nieto, J.M., Sarmiento, A.M., 2006. Evaluation of the dissolved contaminant load transported by the Tinto and Odiel rivers (South West Spain). Appl. Geochem. 21 (10), 1733–1749. https://doi.org/10.1016/j.apgeochem.2006.05.009.

Olías, M., Cánovas, C.R., Macías, F., Basallote, M.D., Nieto, J.M., 2020. The evolution of pollutant concentrations in a river severely affected by acid mine drainage: río tinto (SW Spain). Minerals 10 (7), 598. https://doi.org/10.3390/min10070598.

Paikaray, S., 2021. Environmental stability of schwertmannite: a review. Mine Water Environ. 40 (3), 570–586. https://doi.org/10.1007/s10230-020-00734-2.

Papaslioti, E.M., Giampouras, M., Sánchez-López, L., Basallote, M.D., Freydier, R., Cánovas, C.R., Pérez-López, R., 2024. Temporal dynamics of contaminants in an estuarine system affected by acid mine drainage discharges. Sci. Total Environ. 947, 174683. https://doi.org/10.1016/j.scitotenv.2024.174683.

Park, J., Lee, D., Kim, H., Woo, N.C., 2023. Effects of dry and heavy rainfall periods on arsenic species and behaviour in the aquatic environment adjacent a mining area in South Korea. J. Hazard. Mater. 441, 129968. https://doi.org/10.1016/j.jhazmat.2022.129968.

Parkhurst, D.L., & Appelo, C.A.J. (2013). Description of input and examples for PHREEQC version 3—a computer program for speciation, batch-reaction, one-dimensional transport, and inverse geochemical calculations. In: US Geological Survey Techniques and Methods, Book 6, chap A43, p. 497. https://pubs.usgs.gov/tm/06/a43/.

Parviainen, A., Loukola-Ruskeeniemi, K., Tarvainen, T., Hatakka, T., Härmä, P., Backman, B., Ketola, T., Kuula, P., Lehtinen, H., Sorvari, J., Pyy, O., Ruskeeniemi, T., Luoma, S., 2015. Arsenic in bedrock, soil and groundwater – the first arsenic guidelines for aggregate production established in Finland. Earth Sci. Rev. https://doi.org/10.1016/j.earscirev.2015.03.005.

Pérez-López, R., Nieto, J.M., López-Cascajosa, M.J., Díaz-Blanco, M.J., Sarmiento, A.M., Oliveira, V., Sánchez-Rodas, D., 2011. Evaluation of heavy metals and arsenic speciation discharged by the industrial activity on the Tinto-Odiel estuary. SW Spain. Marine Pollution Bulletin 62 (2), 405–411. https://doi.org/10.1016/j.marpolbul.2010.12.013.

Pérez-López, R., Millán-Becerro, R., Basallote, M.D., Carrero, S., Parviainen, A., Freydier, R., Macías, F., Cánovas, C.R., 2023. Effects of estuarine water mixing on the mobility of trace elements in acid mine drainage leachates. Mar. Pollut. Bull. 187, 114491. https://doi.org/10.1016/j.marpolbul.2022.114491.

Ram, R., Morrisroe, L., Etschmann, B., Vaughan, J., Brugger, J., 2021. Lead (Pb) sorption and co-precipitation on natural sulfide, sulfate and oxide minerals under environmental conditions. Miner. Eng. 163, 106801. https://doi.org/10.1016/j.mineng.2021.106801.

Sánchez-España, J., Yusta, I., Diez-Ercilla, M., 2011. Schwertmannite and hydrobasaluminite : a re-evaluation of their solubility and control on the iron and aluminium concentration in acidic pit lakes. Appl. Geochem. 26, 1752–1774. https://doi.org/10.1016/j.apgeochem.2011.06.020.

Sánchez-Moyano, J.E., Rodríguez-Muñoz, D., García-Asencio, I., 2025. Evaluating environmental programs: long-term monitoring of crustacean assemblages in a polluted estuary. Estuar. Coasts 48 (1), 1–17. https://doi.org/10.1007/s12237-024-01449-1.

Sarmiento, A.M., Nieto, J.M., Olías, M., Cánovas, C.R., 2009. Hydrochemical characteristics and seasonal influence on the pollution by acid mine drainage in the Odiel river Basin (SW Spain). Appl. Geochem. 24 (4), 697–714. https://doi.org/10.1016/j.apgeochem.2008.12.025.

Schoepfer, V.A., Burton, E.D., 2021. Schwertmannite: a review of its occurrence, formation, structure, stability and interactions with oxyanions. Earth Sci. Rev. 221, 103811. https://doi.org/10.1016/j.earscirev.2021.103811.

Shi, M., Min, X., Ke, Y., Lin, Z., Yang, Z., Wang, S., Peng, N., Yan, X., Luo, S., Wu, J., Wei, Y., 2021. Recent progress in understanding the mechanism of heavy metals retention by iron (oxyhydr)oxides. Sci. Total Environ. 752, 141930. https://doi.org/10.1016/j.scitotenv.2020.141930.

Verney, R., le Berre, D., Repecaud, M., Bocher, A., Bescond, T., Poppeschi, C., Grasso, F., 2024. Suspended particulate matter dynamics at the interface between an estuary and its adjacent coastal sea: unravelling the impact of tides, waves and river discharge from 2015 to 2022 in situ high-frequency observations. Mar. Geol. 471, 107281. https://doi.org/10.1016/j.margeo.2024.107281.

Zhang, H., Shikui, Z., Aibin, Z., Yonghua, Z., Zenghui, Y.U., Huaijing, Z., Zenghui, Y., 2015. Heavy metals in suspended matters during a tidal cycle in the turbidity maximum around the Changjiang (Yangtze) Estuary. Acta Oceanol. Sin. 34 (10), 36–45. https://doi.org/10.1007/s13131-015-0675-y.